https://doi.org/10.5194/egusphere-2024-2499
Preprint. Discussion started: 20 August 2024

Climate variability off Africa's southern Cape over the past 260, 000 years

Karl Purcell[1,2,3], Margit H. Simon[4,2,3], Ellie J. Pryor[1,2], Simon J. Armitage[5,2], Jeroen van der Lubbe[6], and Eystein Jansen[1,2,3]

[1]Department of Earth Sciences, University of Bergen, Bergen, 5007, Norway
[2]SFF Centre for Early Sapiens Behaviour (SapienCE), University of Bergen, Bergen, 5020, Norway
[3]Bjerknes Centre for Climate Research, Bergen, 5007, Norway
[4]NORCE, Norwegian Research Centre, Bergen, 5007, Norway
[5]Department of Geography, Royal Holloway University of London, Surrey, TW20 0EX, United Kingdom
[6]Department of Earth Sciences, Vrije Universiteit, Amsterdam, 1081, Netherlands

Correspondence to: Margit Simon (msim@norceresearch.no)

Abstract. During the late Quaternary the past climatic conditions of southern South Africa underwent fluctuations, influenced by various climatic factors, such as the impacts of both the Indian and Atlantic Oceans, as well as the effects of the southeasterly trade winds and Southern Hemisphere Westerlies (SHW), influenced by changes in orbital parameters. At the same time, this region exhibits some of the most abundant Middle Stone Age (MSA) archaeological sites containing records of *Homo sapiens* behavioural and technological evolution. Consequently, there is a pressing need for precise climatic reconstructions that can provide climate constraints during the MSA in this area. However, there is a lack of continuous high-resolution climate records covering the majority of the MSA, which spans from ~300 to ~60 ka. In this study, we present data obtained from a marine sediment core (MD20-3592) that spans approximately the last 260,000 years (from marine isotope stages 8 to 1) aiming to expand the spatial and temporal coverage of available climate archives. This marine sediment core documents both terrestrial and ocean hydroclimate variability because it is strategically positioned close to the South African coastline receiving terrestrial sediments via riverine input as well as being located under the marine influence of the Agulhas Current at the same time. X-ray fluorescence (XRF) core scanning, calibrated with discrete samples analyzed by XRF spectroscopy, was used to determine the variability of the bulk elemental composition of the core over time. Principal component analysis was performed to facilitate the interpretation of the data. Statistical analyses including frequency analysis, gaussian filtering, and wavelet analysis reveal that the regional hydroclimate was affected mostly by local insolation changes caused by orbital precession, and high latitude forcing that varies on timescales associated with orbital obliquity and eccentricity. Increased fluvial input was associated with a high precession index, during times of high local insolation, due to the effects of precession on local convergence and seasonal rainfall. Comparison with regional climate archives confirmed the dominant influence of precession on precipitation in southern South Africa. On glacial-interglacial timescales, lower precipitation observed during glacial intervals could be explained by a northward shift of the

https://doi.org/10.5194/egusphere-2024-2499
Preprint. Discussion started: 20 August 2024

Southern Hemisphere Westerlies (SHW) and South Indian Ocean convergence zone (SIOCZ). Finally, the data from core MD20-3592 can provide a climatic context for the appearance of behavioral complexity in South Africa between ~ 120 ka and ~ 50 ka. Humid conditions in the river catchments going through the south coast and south-east coast of South Africa were present at approximately 117 ka, 93 ka, and 72 ka, alternating with dry conditions at approximately 105 ka, 83 ka, and 60-50 ka.

1 Introduction

Multiple archaeological sites in southern South Africa record the development of behavioural complexity in anatomically modern humans, *Homo sapiens*, between 120 and 50 ka (Wurz, 2012; Fig. 1). This change is inferred from archaeological findings, such as evolving technologies in stone tools from ~ 115 ka to ~ 60 ka (Wurz, 2002) and evidence of hunting projectile technology dating from ~ 63 ka at Klasies River (Bradfield et al., 2020; d'Errico and Henshilwood, 2007), stone tool technology that includes heat treatment in Pinnacle Point and Blombos Cave between ~ 72 and ~ 75 ka (Brown et al., 2009; Mourre et al., 2010), symbolic expression such as pieces of engraved ochre dating from ~ 100 ka to ~ 75 ka and an abstract drawing at Blombos Cave dating from ~ 73 ka (Henshilwood et al., 2009; Henshilwood et al., 2018), and engraved ostrich eggshells at Klipdrift Shelter from ~ 65 to ~59 ka (Henshilwood et al., 2014). These findings highlight shifts towards more complex behaviours that includes signs of abstract thinking, planning depth, innovativeness, and symbolic behaviour (Mcbrearty and Brooks, 2000). The drivers of this critical transformation remain poorly understood, but one frequently suggested mechanism proposes that the complex behavioural changes may have been stimulated by the need to adapt to rapidly changing environmental and climatic conditions (e.g., Bar-Matthews et al., 2010; McCall and Thomas, 2012; Beyin et al., 2023). Verifying this mechanism is complicated by a dearth of high-resolution records available for southern African environmental and climatic change at this time interval (e.g., Chase, 2021). Thus, reconstructing the climatic conditions in southern Africa can help to contextualise the climatic context during this important interval. More specifically, precipitation over this region was highly variable during the last two glacial cycles (Simon et al., 2015) and could have had a major impact on the availability of resources available to early humans in that area.

One aspect of this variability is its impact on vegetation characteristics. During MIS 5b and 4, the coastal lowlands in the eastern Cape province experienced higher summer rainfall and higher abundances of C4 grasses than during MIS 5a and MIS 3 (Braun et al., 2020). Increasing amounts of summer rainfall are associated with an increase in percentage of C4 grasses, likely due to the fact that C4 grasses grow mainly in the summer months (Braun et al., 2020; Cowling, 1983). Both Bar-Matthews et al. (2010) and Ziegler et al. (2013) observed that during the shift towards more summer rains and C4 vegetation at 72 ka (MIS 4), there was a coincident increase in preference for using silcrete to produce tools, potentially indicating broadened trading networks (Deacon, 1989). Along coastal environments, a strong influence of the Agulhas Current on hydroclimate is apparent (Chase and Quick, 2018), while solar insolation changes linked to orbital precession

https://doi.org/10.5194/egusphere-2024-2499
Preprint. Discussion started: 20 August 2024

(23-19 ka cycles) seemed to have a stronger impact on vegetation inland (Braun et al., 2020). Higher summer insolation in the Southern Hemisphere (SH) is thought to strengthen the continental heat low and thus increase tropical temperate throughs and convective rainfall over the southern coast of South Africa (Braun et al., 2020). Changes in orbital obliquity (41 ka cycles) might also have affected precipitation over this region, by influencing the cross-equatorial insolation gradient and transport of moisture (Bosmans et al., 2015; Daniau et al., 2023). Orbital eccentricity (100 ka cycles) could likewise have played a role by amplifying or reducing seasonality, and thus modulating direct insolation (Maslin and Ridgwell, 2005). Furthermore, the African climate was subject to high-latitude forcing, which varied primarily on glacial-interglacial timescales linked with changes in orbital obliquity and eccentricity (de Menocal et al., 1993).

The hydroclimate of southern Africa is recorded in multiple terrestrial and marine climate archives (e.g., Chase, 2021). However, the southern part of South Africa is poorly resolved, especially on orbital timescales (Fig. 1). So far, to the author's best knowledge, there are no published marine sediment cores records offshore the Southern Cape which span the last two glacial cycles. This study aims to provide the first high-resolution and continuous record of terrestrial climate and palaeoceanographic conditions for the study region using core MD20-3592, a new marine sediment core retrieved off the coast of southern South Africa in 2020 (Fig. 1). The objectives are (1) to characterise the provenance of the climate signal, (2) to construct a hydroclimatic proxy record for this region covering the last 250 ka, and (3) to investigate the drivers of hydroclimatic variations on glacial/interglacial and orbital timescales.

https://doi.org/10.5194/egusphere-2024-2499
Preprint. Discussion started: 20 August 2024

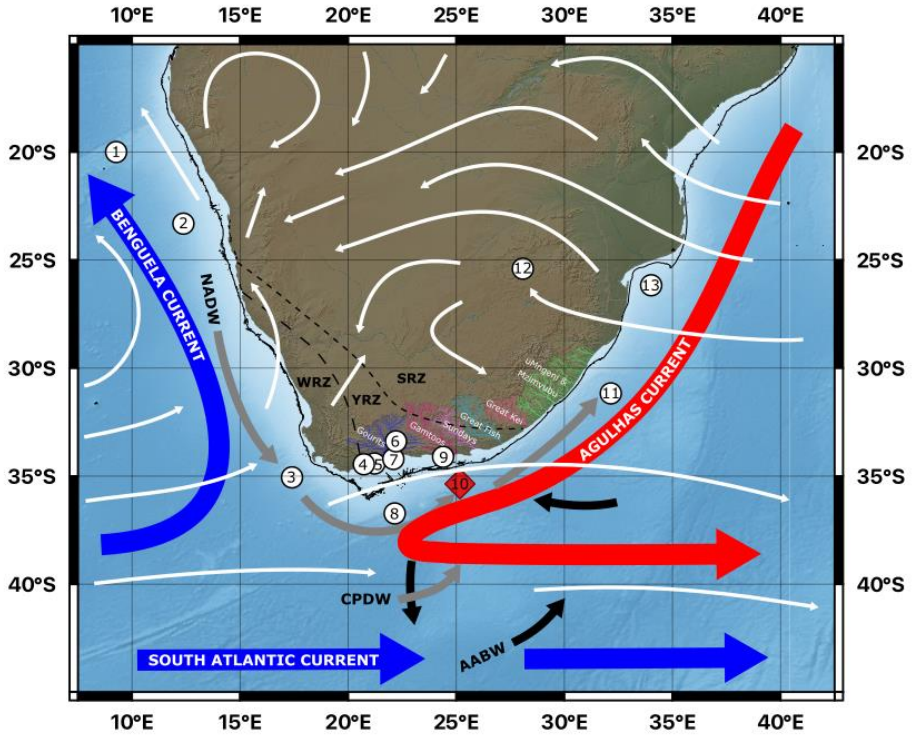

Figure 1. Locations of study core, climatic archives, and archaeological sites in South Africa. The Winter Rainfall Zone (WRZ), Year-round Rainfall Zone (YRZ) and Summer Rainfall Zone (SRZ) are shown and delimited by dashed lines (Hahn et al., 2021a). The -130 m isobath (LGM shoreline: Cawthra et al., 2020) is indicated by a black line. Dominant surface winds are represented by white arrows, surface currents by blue (cold) and red (warm) arrows, deep water flow by grey arrows (NADW, North Atlantic Deep Water; CPDW, Circumpolar Deep Water), and bottom water flow by black arrows (AABW, Antarctic Bottom Water) [Van Aken et al. (2004), Franzese et al. (2009), Chase (2021)]. Relevant river basins are highlighted in colours along the Western Cape, the Eastern Cape, and the KwaZulu-Natal province. Study core MD20-3592 is shown with a red diamond, while other paleo-climatological and archaeological sites mentioned are indicated by white circles: (**1**)- Core MD96-2094 (Stuut et al., 2002), (**2**)- MD08-3167 (Collins et al., 2014), (**3**)- Cores at IODP site U1479 (Dupont et al., 2022), (**4**)- Klipdrift shelter cave site (Henshilwood et al., 2014), (**5**)- Blombos cave site (Henshilwood et al., 2011), (**6**)- Cango Caves (Chase et al., 2021), (**7**)- Pinnacle point (Brown et al., 2009), (**8**)- MD20-3591 (Pryor et al., 2024), (**9**)- Klasies river caves (d'Errico and Henshilwood, 2007), (**11**)- CD154 10-06 P (Simon et al., 2015), (**12**)- Tswaing Crater (Partridge et al., 1997), (**13**)- MD96-2048 (Caley et al., 2018).

2 Regional setting

In this study, we analysed the marine sediment core MD20-3592 (35 °21.726'S; 25 °10.302'E; 4078 m water depth; Fig. 1) which was retrieved in the southwest Indian Ocean during the MD225 ACCLIMATE-2 Cruise of the R/V Marion Dufresne

https://doi.org/10.5194/egusphere-2024-2499
Preprint. Discussion started: 20 August 2024

(Vazquez Riveiros and Waelbroeck, 2020). The core site is situated beneath the surface Agulhas Current, on the bottom of the Agulhas Passage, a channel that is bounded by the Agulhas Bank to the north and the Agulhas Plateau in the south (Uenzelmann-Neben, G. and Huhn, K., 2009). The core is located offshore a number of well documented archaeological sites (Fig. 1) and is therefore an ideal candidate to reconstruct terrestrial climatic conditions experienced at coastal sites such as Klasies River Main, Blombos Cave, Pinnacle point and Klipdrift Shelter, while marine proxy records provide age constraints and palaeoceanographic conditions.

A study on sediment provenance indicated that the sediments near the study site (Fig. 1) are mostly from local terrestrial sources and from eastern South Africa brought via the Agulhas Current (Franzese et al., 2009). Six major rivers discharge their sediments from the South African continental margin into the ocean near the study site: the Gourits river in the western Cape Province, and the Gamtoos, Sundays, and Great Fish River in the eastern Cape Province, and the Umgeni and Mzimvubu rivers in the KwaZulu-Natal Province (Fig. 1). These rivers are the closest sources of terrestrial inputs to the South African continental margin, and the variability in their sediment bulk composition can record fluctuations in sediment input, and variations in sediment input from these sources result from changes in rainfall amount in their catchments (Simon et al., 2015). The mouths of the rivers mentioned above in the Western and Eastern Cape are at present between ~150 and ~400 km away from site MD20-3592. However, during periods of lower sea levels such as the LGM (see Fig. 1), their course would have been extended seaward up to 100 km, bringing the river mouths much closer to the core site (Cawthra et al., 2020). Accordingly, changes in sediment composition observed throughout the core can be interpreted as indicating changes in the sediment supply to the core from nearby river catchments (i.e. rainfall amount), or in distance of the coring site to the river mouths (i.e. eustatic sea-level change). Franzese et al. (2006) observed an increased proportion of local southern African sources during the LGM in sediments near the study site.

The river catchments of the Gourits, Gamtoos, Sundays, and Great Fish are in great part in the year-round rainfall zone (YRZ), a region which receives approximately equal precipitation during the winter and summer months (Fig. 1). This zone, which covers the southern Cape coast and parts of the Western Cape, is located between the summer rainfall zone and the winter rainfall zone, and therefore receives both summer and winter precipitation (Chase and Meadows, 2007; Fig. 1). The Gamtoos, Sundays, Great Fish, Great Kei, and Umngeni & Mzimvubu rivers are located in part or totally in the summer rainfall zone (SRZ), where over 66% of the rain falls between October-March (Fig. 1). Most of the rain in this zone can be attributed to the SIOCZ, which is a band of enhanced precipitation that extends from southern Africa into the southwest Indian Ocean, from 10°–40°S to 0°–60°E (Cook, 2000; Hahn et al., 2021b; Lazenby et al., 2016). Rainfall from the Indian Ocean is brought eastward by tropical temperate troughs (TTTs), which form at the SIOCZ (Hahn et al., 2021b; Jury et al., 1993; Reason and Mulenga, 1999). These subtropical systems are driven by high sea surface temperatures (SST) and warming of the continents during the summer to establish strong convections cells (Chase and Meadows, 2007). The winter rainfall zone (WRZ), with over 66% of its precipitation occurring between April and September, is located along the western

https://doi.org/10.5194/egusphere-2024-2499
Preprint. Discussion started: 20 August 2024

coast of the Western Cape (Fig. 1). It receives moisture from the Atlantic Ocean brought by temperate frontal systems linked to the SHW (Chase and Meadows, 2007).

A smaller proportion of the sediments near the study site has been found to originates from the Southwest Atlantic, and this portion is thought to be brought by deep-waters (Franzese et al., 2006), namely Antarctic bottom water (AABW) and North Atlantic deep water (NADW) which flows through the Agulhas Passage from southwest to northeast (Uenzelmann-Neben and Huhn, 2009; Fig. 1). Another potential source of terrigenous sediments to the study site is aeolian dust, however the southern coast of South Africa currently receives less than 1 g/m^2/year of aeolian dust, and up to 10 g/m^2/year during dustier intervals such as the Last Glacial Maximum (LGM) (Maher et al., 2010). This represents ~ 1 to ~ 7 % of the inferred sediment accumulation rate at the study site (142 g/m^2/year; see section 4.2.2).

3 Materials and Methods

3.1 Elemental composition measurement

3.1.1 XRF core scanning

XRF scanning was performed to quantify the changes in the geochemical characteristics of the sediment with a 2 mm resolution, using an ITRAX core scanner from Cox Analytics (Croudace et al., 2006). Previous studies have used variations in sediment geochemistry (e.g., Govin et al., 2012; Ziegler et al., 2013; Hahn et al., 2021b) to infer changes in the rate of marine versus terrestrial deposition, or the rate of physical and chemical weathering, which can be interpreted as resulting from changes in terrestrial rainfall. The elemental count rates were normalized against the sum of the total incoherent and coherent scattering to eliminate the imprint of down-core variations in the water content and organic components (Kylander et al., 2011; Davies et al., 2015). Log ratios of the element intensities were calculated since they provide the most easily interpretable signal of relative change in chemical composition, because they avoid the problem of non-linear matrix effects and constant sum constraints (Weltje and Tjallingii, 2008; supplementary material).

3.1.2 XRF calibration

The qualitative XRF data can be calibrated to give quantitative results, and thus constrain the magnitude of change, the interpretation of proxies and the paleoclimatic information derived from sediment cores (Dunlea et al., 2020). 20 discrete samples were selected for calibration throughout the core to represent the full range of elemental XRF intensity. Major elements (Al, B, Ba, Ca, Co, Cr, Cu, Fe, K, Li, Mg, Na Mn, Ni, P, Pb, S, Sr, Ti, V, Y, Zn, Zr) were measured using a Thermo Scientific ICap 7600 Inductively Coupled Plasma Atomic Emission Spectrometer (ICP-AES) at the University of

https://doi.org/10.5194/egusphere-2024-2499
Preprint. Discussion started: 20 August 2024

Bergen. Trace elements (Ba, Co, Cr, Cs, Cu, Hf, Li, Mn, Nb, Ni, Pb, Rb, Sc, Sr, Ta, Th, Ti, U, V, Y, Zn, Zr, Ge, Mo and others) were measured with a Thermo Scientific Element XR High-Resolution Inductively Coupled Plasma Mass Spectrometer (HR-ICP-MS).

18 of the 20 discrete samples were sub-sampled for XRF bulk chemistry analysis at the Vrije Universiteit Amsterdam (VU), with the samples at 512 cm and 660 cm depth having too little remaining material (See Table 1 and S1). The bulk sediments were dried at 110°C and subsequently powdered using an agate ball mill. About 1 gram of dried sample powder was ignited at 1000°C for 45 minutes, which allows to determine the loss on ignition (LOI). Hereafter, the samples powders were mixed with $Li_2B_4O_7/LiBO_2$ with a 1:4 dilution and fused to glass beads. The concentrations of major elements (Fe, Mn, Ti, Ca, K, P, Si, Al, Mg, Na, Ba) were subsequently measured by X-ray fluorescence spectroscopy (XRF) on a PANalytical Axios mAX instrument. The oxide concentrations were derived from the interference corrected major element spectra using a calibration curve based on 28 international standards. The major element data were normalised to 100% with Fe expressed as Fe_2O_3. Using these concentrations, a log ratio calibration was conducted for the XRF core scanning data to obtain quantitative ratios by using the log-ratio calibration described by Dunlea et al. (2020), with calcium as the common denominator because this element gave the best calibration results in Weltje and Tjallingii (2008).

3.1.3 Principal component analysis

Principal component analysis (PCA) was conducted to facilitate interpretation of the XRF data. The application of this method on XRF data from marine sediment cores has been shown to provide insight into geochemical and physical variability (Taylor et al., 2022). PCA was used on the elements with the strongest XRF counts and with an environmental significance: Ti, Fe, Rb, Si, K, Zr, Al, Sr, and Ca. It was performed with the "prcomp" function in the R programming language (R Team, 2019). PCA is a method that reduces dimensionality by transforms a large number of variables into a smaller number, while still containing most of the information. The analysis produces principal components, new variables which are a linear combination of the initial variables. Each component is created to represent the maximum variance observed in the data set, while the components are uncorrelated between themselves. The first principal component represents the highest variance, while each subsequent component represents a lower variance in the data set. Each component is calculated with a column matrix containing the loadings. These are the values representing the weight and sign of the contribution of each variable to a particular principal component (see Fig. 7 for clarification). In order to perform the PCA, the prcomp function does a singular value decomposition, which is optimal for numerical accuracy (R Team, 2019). The values for each element first had their means centred to zero and their variance set to one, so as to avoid elements with larger ranges of intensities to dominate the analysis.

https://doi.org/10.5194/egusphere-2024-2499
Preprint. Discussion started: 20 August 2024

3.2.5 Spectral analysis

After transferring the PC1 record onto age, the record was interpolated to the average age time step of 11.4 years with the Acycle MATLAB package (Li et al., 2019) to obtain equally-spaced time-series. Subsequently, the data was detrended using the 2nd order detrending method in Acycle to prevent power leakage from low frequency components into higher frequencies of the spectrum (Li et al., 2019). Below are the following steps used to perform spectral analysis:

1) To detect dominant temporal frequencies, the power spectra of PC1 on age was calculated with the periodogram function in Acycle (Li et al., 2019). An autoregressive AR(1) red noise model was fitted to the spectrum to determine, which peaks are significantly different from noise, with 90%, 95% and 99% confidence limits.
2) Gaussian filtering using the dominant frequencies found in 1) were then applied to PC1 using Qanalyseries (Kotov and Pälike, 2018) to determine whether the dominant frequencies observed in the data are in phase with the cyclical changes to the Earth's orbital parameters.
3) Wavelet analysis on PC1 was conducted to allow visualization of its temporal evolution with the Continuous Wavelet Transform (CWT) function in the Wavelet coherence MATLAB toolbox (Grinsted et al., 2004).

More information on these steps can be found in the supplementary material.

4 Results

4.1 Elemental composition measurement

4.1.1 X-ray fluorescence (XRF) core scanning

Terrestrial elements (Al, Si, K, Ti, Fe) on calcium are depicted in Figure 2b-f and Fe/K (Figure 2g). Over the entire core depth from 0 to 45 m there is no apparent long-term trend, although the general pattern displays variability, with notable peaks towards higher values found in the 12-20 m and 32-40 m depth intervals for all elemental ratios (Figure 2) (note: axis values are in reverse order). Low counts are recorded for all ratios between 20-30 m. These ratios are expected to vary in tandem when there are variations in the amount of terrigenous material carried to the site from regional river discharge. Fe/K (Figure 2g) varies in a comparable pattern with the other elemental ratios. This can be explained by peaks in this ratio indicating physical and/or chemical weathering, as high sedimentary Fe/K values reflect more fluvial or aeolian input of intensively weathered material from humid areas in the source region to the coring site (Govin et al., 2012). This ratio has the advantage of being independent of variations on Ca concentration, which can be influenced by marine processes. In tropical humid regions, high Fe/K is the result of high chemical weathering or high soil erosion, which can both be caused by increased precipitation (Ziegler et al., 2013). Increased weathering of clay minerals has the effect of enriching the soil in iron, and thus rivers originating in regions with increased weathering transport more iron towards the ocean. Additionally, increased soil erosion due to increased precipitation can also increase the Fe/K ratio in marine sediments. It is to be noted

https://doi.org/10.5194/egusphere-2024-2499
Preprint. Discussion started: 20 August 2024

that soil erodibility can also be increased by less protection from lower vegetation cover (Ludwig and Probst, 1998). In the case of the K, its primary source is from potassium feldspar or illite that are typical of a drier climate with low chemical weathering (Zabel et al., 2001). In addition, it can be observed that Al has the highest variability among all the plotted ratios. This is probably due to its low signal strength, as light elements such as Al have a low X-ray yield in XRF scanning and are most susceptibility to X-ray absorption effect by pore water and water at the core surface under the plastic foil applied during scanning.

https://doi.org/10.5194/egusphere-2024-2499
Preprint. Discussion started: 20 August 2024

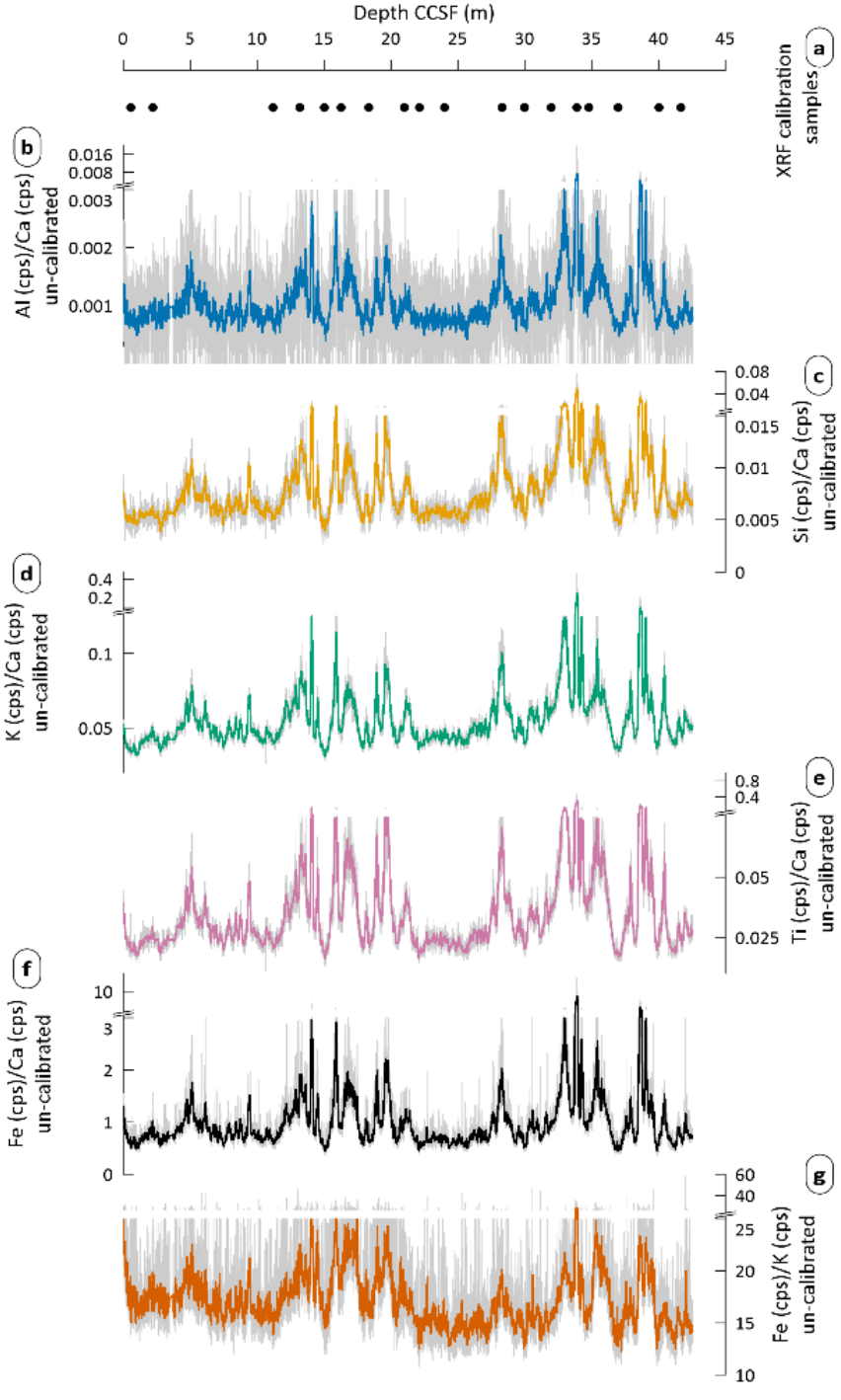

Figure 2. Ratios of selected element intensities. (**a**) Location of samples used for calibration. (**b-g**) Ratios of selected elements. Pale grey is full resolution measurements, while dark colours are 21 point running means: Al/Ca in blue, Si/Ca in yellow, K/Ca in green, Ti/Ca in

https://doi.org/10.5194/egusphere-2024-2499
Preprint. Discussion started: 20 August 2024

purple, Fe/Ca in black, and Fe/K in orange. Lower variability in d and e causes the running average to overlap closely with the full resolution.

4.1.2 XRF calibration

235 The values of selected element oxides in the 18 calibration samples measured at VU are shown in table 1, and the 20 samples measured in Bergen can be seen in table S1. The results from VU were chosen for calibration because they included SiO_2 which is the most abundant oxide in core MD20-3592. The 18 replicate samples measured by both methodologies had results on average within 11% of each other, with 1σ below 4% for the elements used for calibration. Silicon could not be compared, and potassium exhibited a larger variation (1σ =15%).

240 The sediments are hemipelagic, with a large proportion of terrigenous material and a relatively lower amount of carbonate. It can be observed that at the depths where the concentration for CaO is the lowest, notably at 1320 cm, 2832 cm, and 3390 cm, the other elemental oxides have the highest concentrations (Table 1). The measurements of the 18 samples were used to calibrate the log ratios of the XRF intensities to quantitative ratios.

https://doi.org/10.5194/egusphere-2024-2499
Preprint. Discussion started: 20 August 2024

Depth interval (cm)	Al_2O_3 (g/kg)	SiO_2 (g/kg)	K_2O (g/kg)	TiO_2 (g/kg)	Fe_2O_3 (g/kg)	CaO (g/kg)
56-57	71.9	348.0	7.4	4.0	29.0	261.1
220-221	51.5	238.6	3.7	2.7	22.7	145.4
1120-1121	70.0	348.9	5.5	3.9	30.9	260.3
1320-1321	98.7	458.5	11.6	5.3	44.2	157.8
1504-1505	65.2	317.6	4.5	3.6	26.4	288.7
1628-1629	83.8	395.7	9.2	4.6	33.7	220.6
1836-1837	72.6	356.5	5.4	4.0	29.2	258.1
2100-2101	95.3	420.9	8.2	5.0	36.7	196.9
2212-2213	72.6	330.6	5.8	3.7	31.5	274.0
2400-2401	75.7	370.7	6.4	4.1	32.5	245.6
2832-2833	114.0	484.8	15.1	5.7	54.6	129.4
3000-3001	72.5	361.7	9.2	4.0	28.8	252.7
3200-3201	90.2	417.1	9.5	4.9	38.2	200.8
3390-3391	135.3	575.1	22.7	7.1	56.3	51.3
3480-3481	92.3	472.8	9.7	5.7	36.1	174.0
3700-3701	70.0	340.1	7.3	3.9	34.5	282.7
4002-4003	75.0	408.1	7.8	4.2	25.4	231.6
4166-4167	79.7	373.4	7.5	4.1	34.4	236.8

Table 1. Measured concentrations in g/kg of selected element oxides for the calibration samples.

In Fig. 3a, the log ratio of the element percentages measured with ICP-AES/MS are plotted against the log ratios of average XRF counts at the same depth intervals. The linear regression displays a good fit between the two log ratios, with a r^2 value ranging from 0.94 to 0.99. The linear regression equation (1) is used to calibrate the log ratio of XRF counts, where "x" is the natural logarithm of the elemental ratios of XRF intensities. This gives a calibrated log ratio.

$$y=ax + b \quad \text{Equation (1)}$$

To obtain a simple quantitative ratio, equation (2) is applied:

$$[Ratio=E^{(log\text{-}ratio)}] \quad \text{Equation (2)}$$

Combining equations (1) and (2) gives equation (3):

$$Ratio = E^{(ax + b)} \quad \text{Equation (3)}$$

where x is the uncalibrated log-ratio. The calibrated elemental ratios are plotted against the measured elemental ratios in Fig. 3b. Using the calibration equations (see supplementary material), the selected elemental ratios where calculated and shown

https://doi.org/10.5194/egusphere-2024-2499
Preprint. Discussion started: 20 August 2024

in Fig. 4. The resulting calibrated ratios show similar trends with the XRF intensities ratios of Fig. 2, with the notable difference of some major peaks appearing much larger in comparison to the general variability. This shows that the calibration yields effective individual elemental concentrations.

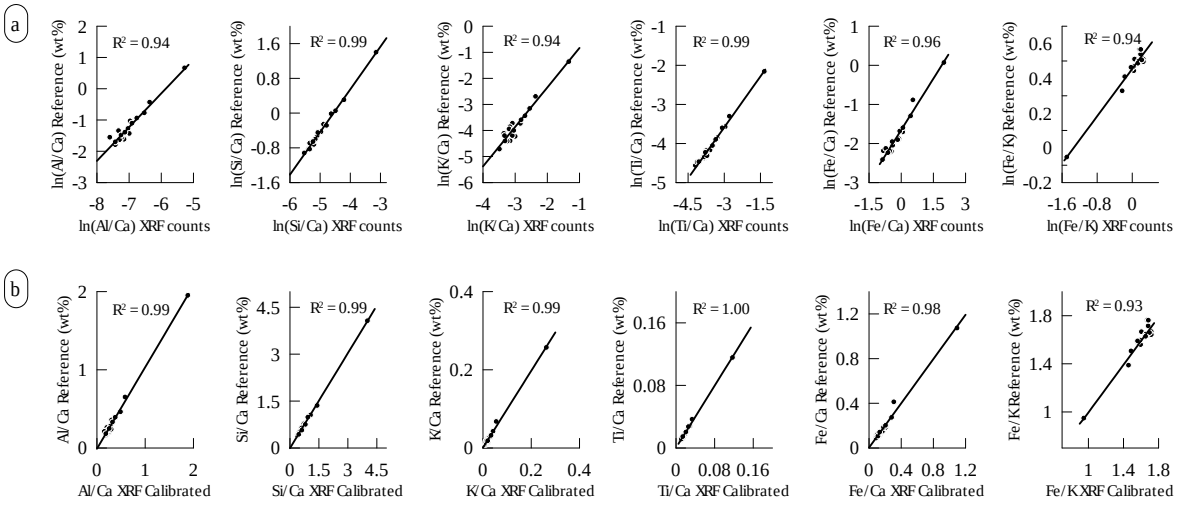

Figure 3. Log calibration data. (**a)** Log ratio of elemental concentrations measured by ICP-AES and ICP-MS (wt%) versus the log ratio of XRF counts (cps). (**b)** Ratio of oxide concentrations calculated from the ICP-AES and ICP-MS measurements versus the calibrated oxide ratios calculated from the XRF measurements. The r^2 values are reported within each plot, and the 95% confidence interval for the slope is displayed in grey shading. The calibration equations were subsequently used to calibrate the log ratios for the whole length of the core (Fig. 4).

https://doi.org/10.5194/egusphere-2024-2499
Preprint. Discussion started: 20 August 2024

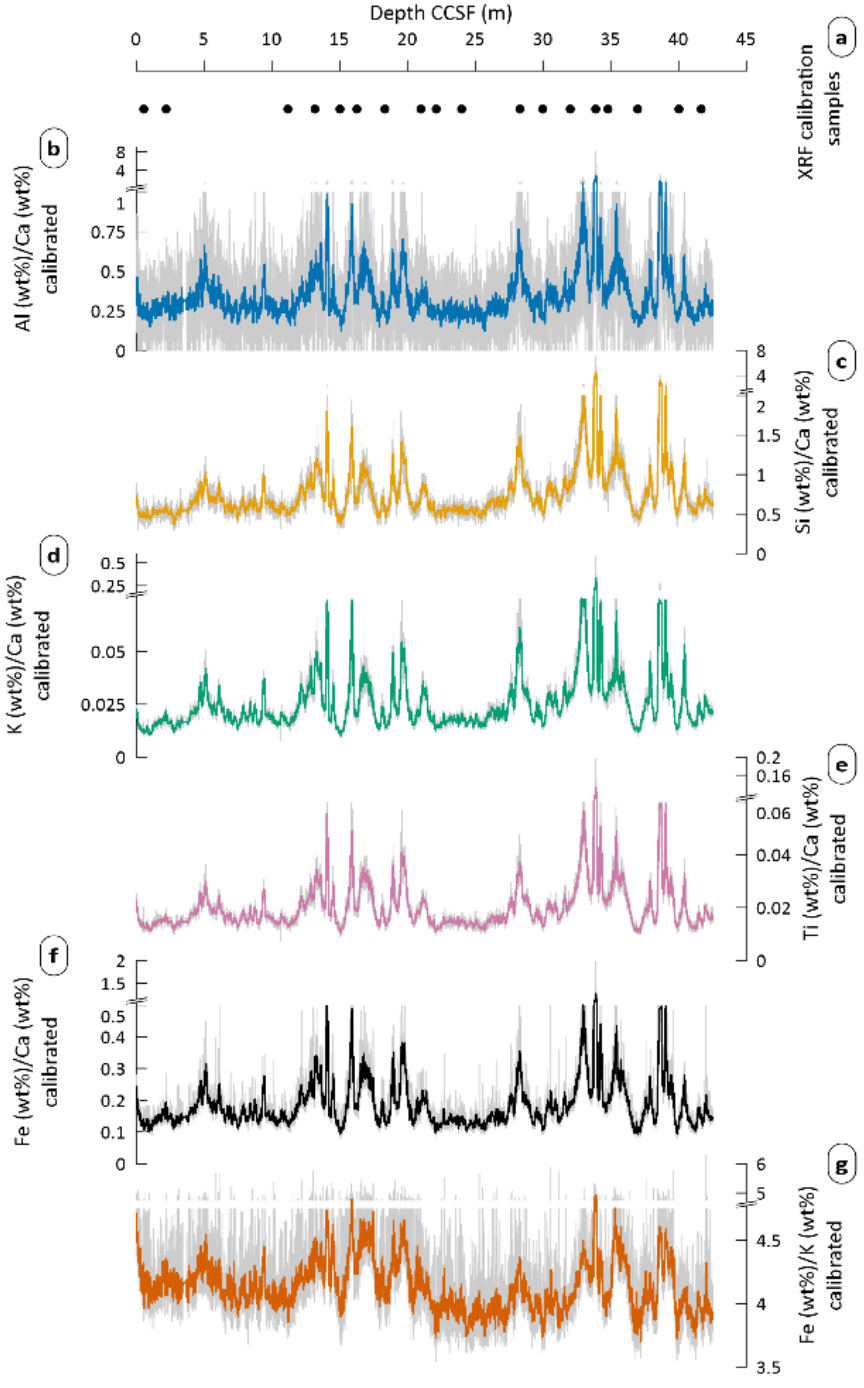

Figure 4. Elemental ratios after log calibration. (**a)** Location of samples used for calibration. (**b-f)** Elemental ratios of selected elements. Pale grey is full resolution measurements, while dark colours are 21 point running means: Al/Ca in blue, Si/Ca in orange, K/Ca in green,

https://doi.org/10.5194/egusphere-2024-2499
Preprint. Discussion started: 20 August 2024

Ti/Ca in purple, Fe/Ca in black, and Fe/K in vermillion. Lower variability in d and e causes the running average to overlap closely with the full resolution.

4.2 Age modelling

4.2.1 Methodology

For the uppermost 50 ka in the core, the age model shown in Fig. 5 and 6 is based on 14 radiocarbon dates of planktonic foraminifera (*Globigerinoides ruber*) (See table 2). The samples contained around 1 to 2 mg of material (> 250–315 μm). Accelerator mass spectrometry (AMS) analyses were conducted at the ETH Zurich radiocarbon laboratory, Switzerland. To calibrate individual radiocarbon dates for the upper portion of the core, we used the Marine20 radiocarbon age calibration curve (Heaton et al., 2020), with a local reservoir correction (ΔR) of 36 ± 35 years based on the nearest 5 measured points (Reimer and Reimer, 2001). Calibration of the radiocarbon dates was performed with the Bayesian ^{14}C calibration software *MatCal* (Lougheed and Obrochta, 2016). The uncertainty on the radiocarbon dates is indicated in Table 2.

Beyond the age range of radiocarbon, the chronology of core MD20-3592 is obtained by matching the pattern of planktic foraminifera $\delta^{18}O$ record with the δD record of EDC (Bazin et al., 2013; Veres et al., 2013). The planktonic $\delta^{18}O$ record reflects the combined influences of local sea-surface temperature and $\delta^{18}O$ seawater fluctuation and global ice volume changes, while the δD reflects the past air temperatures in Antarctica. These two records can be well matched with a relatively small number of tie points (n = 5), and thus allows to create an age model for core MD20-3592 based on the chronology of EDC. The $\delta^{18}O$ curve is therefore graphically correlated with the EDC δD record using 5 tie points. The tuning points are located at sharp climatic transitions; the beginning of MIS 4 (70.9 ka), the end and beginning of MIS 5e (112.6 and 132.8 ka), and at the end and beginning of MIS 7 (198.5 and 246.1 ka) (Fig. 6). Samples were taken every ~8 cm, with ten specimens of *G. ruber* from size fraction 212-355 μm picked per analysis. However, in intervals of lower abundance of *G. ruber*, *Neogloboquadrina* was also sampled in order to measure them if the amount of *G. ruber* for these intervals was found to be too low for analysis. Lower abundance could come from less optimal growing conditions for *G. ruber*, for example during cold periods with colder and fresher waters originating from the Southern Ocean (Simon et al., 2013). Post-depositional processes can also influence the preservation of shells, potentially having a dissimilar effect on different foraminifera species. Notably, the first tie point is made using shells of *N. incompta* instead of *G. ruber*. This was done due to the *G. ruber* data having quite a noisy signal, with high variability in the depth intervals thought to cover the transition from MIS 5 to MIS 4. The *N. incompta* is by contrast displaying a more evident transition in this interval around 70.9 ka than G. ruber, and thus facilitated the graphical correlation between the foraminifera $\delta^{18}O$ record and the EDC δD record. The $\delta^{18}O$ and $\delta^{13}C$ values were obtained using a Finnigan MAT253 MS at FARLAB at the Department of Earth Science at the

https://doi.org/10.5194/egusphere-2024-2499
Preprint. Discussion started: 20 August 2024

University of Bergen. The results are reported relative to Vienna Pee Dee Belemnite (VPDB), expressed as the average of the replicates, calibrated with NBS-19, and independently checked using NBS-18. Long-term repeatability (1 SD) of internal standards aggregated across weeks to months ≤ 0.08 for $\delta^{18}O$ and ≤ 0.03 for $\delta^{13}C$, for samples between 15 and 100 mg.

Using the Bayesian age-depth modelling program "*Undatable*" (Lougheed and Obrochta, 2019), age-depth relationships were created, taking into consideration the age and depth uncertainty of the ^{14}C dates and $\delta^{18}O$ chronological markers (Fig. 6). For the radiocarbon ages, the depth uncertainty covers the depth interval of the sediments sampled for each age, and the laboratory mean ^{14}C ages are calibrated to an age distribution using the embedded *MatCal* function (Lougheed and Obrochta, 2016). For the $\delta^{18}O$ tie-points, the depth uncertainty is represented as a Gaussian function centred on the chosen tie point depth and a 1σ equal to the sampling resolution (8 cm), and the age uncertainty is estimated with the uncertainty reported for the nearest point on the EDC record (Bazin et al., 2013; Veres et al., 2013). Gaussian uncertainty is the best practice when tuning a sequence to a reference record and the exact depth of the feature cannot be determined precisely (Lougheed and Obrochta, 2019). Undatable calculates a probability density function (PDF) for each age marker with the data entered. Then simulations of the age model are performed with random sampling of the PDF of the age points. Afterwards, the program does bootstrapping of these sampled ages, removing at random a specified percentage of the age markers. Age-depth reversals, (i.e., negative sediment accumulation rates) are subsequently removed. Next, an interconnecting point is inserted between the remaining age depth constraints, to take into account the increased uncertainty that comes with distance from the age-depth constraints. This whole cycle is repeated a number of times which results in a probability density cloud of all the age-depth simulation runs. The default values for the "xfactor" and bootstrapping percentage were set to 0.1 and 30%, respectively, and 10^5 simulations were used. The average mass accumulation rate was calculated by multiplying the average density by the average sedimentation rate.

4.2.2 Age-depth model results

The 14 radiocarbon dates indicate that the first 9.13 meters of the core cover approximatively 47.3 ka (Table 2), giving an average sedimentation rate of ~19.3 cm/ka. The sedimentation rates obtained from the uppermost 9.13 meters in the age model (Fig. 5) vary between 8.7 and 48 cm/ka, with the highest sedimentation rates occurring between 304.5 and 456.5 cm, and the lowest rates near the top and bottom of this portion of the core. Apparently anomalous radiocarbon ages are observed at 16 and 23.5 cm depth respectively, with ages older than the age model created with *Undatable*. They could be due to bioturbation, as is suggested by a dark elliptical shape seen around 22 cm depth in the core (Fig. S4). The age modelling using *Undatable* assumes a positive sedimentation rates and will exclude age constraints outside of 2 sigma of the simulated age model (Lougheed and Obrochta, 2019). There is a close visual correspondence between the $\delta^{18}O$ values on the radiocarbon-based age model and the EDC δD values from the Antarctic EDM ice core, which comes from the Antarctic sector to the South of the coring site. This supports the use of graphical correlation between the two records to provide an

https://doi.org/10.5194/egusphere-2024-2499
Preprint. Discussion started: 20 August 2024

age model for the lower portions of MD20-3592. Further downcore, the age model obtained from the $\delta^{18}O$ gives an age of 246.1 ka at a depth of 4068.5 cm, giving an average sedimentation rate of 16.5 cm/ka, or a mass accumulation rate of ~14.2 g/cm^2/ka.

	Uncalibrated age		Calibrated age				Undatable Age model
Depth interval (cm)	^{14}C uncalib. (yr BP)	Uncertainty (yr BP)	From (yr BP)	To (yr BP)	%	Median (yr BP)	Median age (yr BP)
1-3	2613	77	1834	2324	95.4	2081	2090
15-17	10420	100	11112	11769	95.4	11408	3500
23-24	7236	92	7269	7709	95.4	7494	4247
56-57	6780	79	6797	7273	95.4	7048	7082
120-121	9870	91	10303	11009	95.4	10637	10640
192-193	12960	123	14105	15032	95.4	14589	14524
304-305	16810	247	18765	20006	95.4	19353	19248.5
456-457	19520	184	22157	22995	95.4	22584	22657
560-561	23170	254	25951	27078	95.4	26525	26516.5
648-649	25960	335	28648	29992	95.4	29322	29465
686-687	28830	382	31229	33191	95.4	32184	31640.5
752-753	32110	649	34409	37332	95.4	35763	35617
824-825	34428	677	36824	39958	95.4	38453	38793.5
912-913	44170	2663	42917	52900	90.2	47255	46341

Table 2. AMS radiocarbon analyses on *G. ruber* from core MD20-3592. For calibration the Marine 20 curve (Heaton et al., 2020) was used with ΔR of 36 ± 35 years.

https://doi.org/10.5194/egusphere-2024-2499
Preprint. Discussion started: 20 August 2024

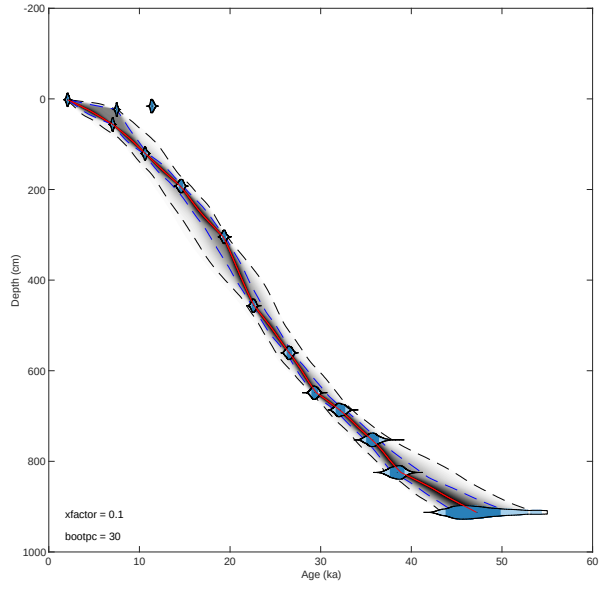

Figure 5. Age-depth model produced using "Undatable" (Lougheed and Obrochta, 2019) for the radiocarbon dates in core MD20-3592. The bootstrapping was set to 30% and sedimentation rate uncertainty set to 0.1. The radiocarbon dates are represented by blue probability density functions, with the deep blue representing 1σ and the light blue 2σ uncertainty. The grey shaded areas indicate probability density for the age-depth model, with darker colours indicating higher age-depth probabilities. Blue and black dashed lines represent 68.27% and 95.45% confidence intervals, respectively. The red line shows the age-depth model median. An age reversal is observed around 7 ka, with the older age exerting less influence in the age model. An additional reversal is observed around 10 ka, but here an age is excluded from the model as an outlier.

https://doi.org/10.5194/egusphere-2024-2499
Preprint. Discussion started: 20 August 2024

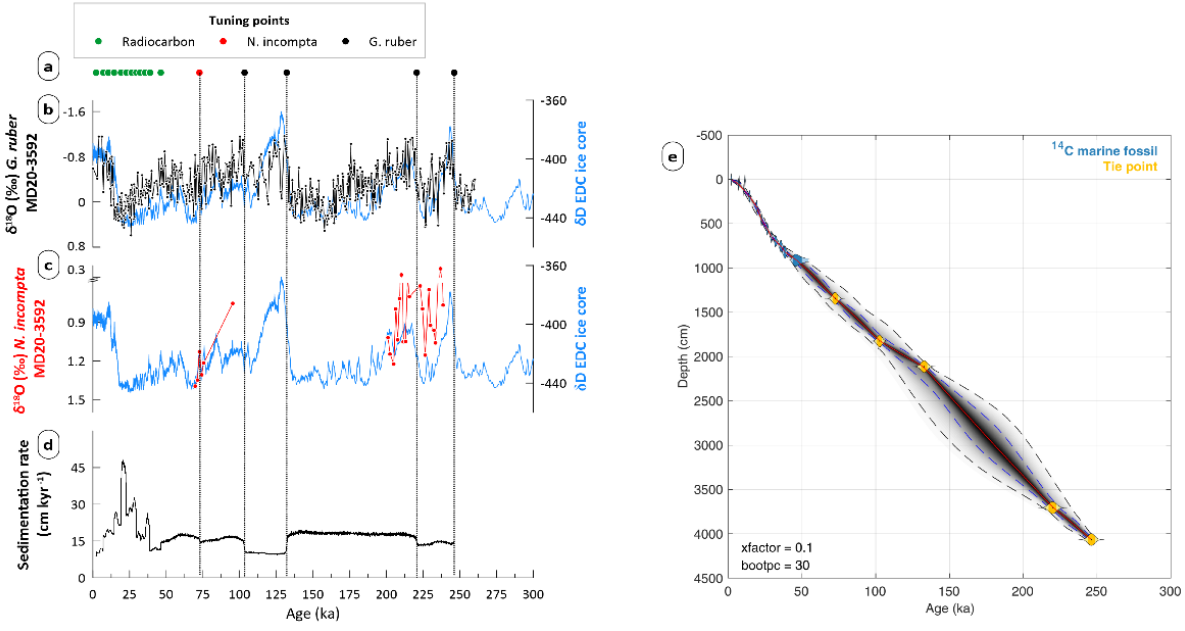

Figure 6. Age model for core site MD20-3592. (**a**) Age control points: radiocarbon dates in green, *N. incompta* $\delta^{18}O$ in red, and *G. ruber* $\delta^{18}O$ in black. (**b**) Graphical correlation of *G. ruber* $\delta^{18}O$ (black line) with the EDC δD record (blue line) on the AICC2012 chronology (Bazin, 2013; Veres, 2013). (**c**) Graphical correlation of *N. incompta* $\delta^{18}O$ (red line) with the EDC δD record (blue line) on the AICC2012 chronology (Bazin, 2013; Veres, 2013). (**d**) Sedimentation rate calculated with "*Undatable*". (**e**) Age-depth model produced for MD20-3592 with "*Undatable*". The bootstrapping was set to 30% and sedimentation rate uncertainty set to 0.1. The radiocarbon dates are represented by blue probability density functions, with the deep blue representing 1σ and the light blue 2σ uncertainty. The tie points from the $\delta^{18}O$ are represented by yellow density function, with the deep yellow representing 1σ and the light yellow 2σ uncertainty. The grey clouds indicate probability density for the age-depth model, with darker colours indicating higher age-depth probabilities. Blue and black dashed lines represent 68.27% and 95.45% confidence intervals, respectively. The red line shows the age-depth model median.

4.3 Principal component analysis

The first principal component (PC1) explains the majority of the variance in the XRF record (~60%; Fig. 7) and was thus retained for further examination. It is marked by positive loadings of Ti, Fe, Rb, Si, K, Zr, Al, and the negative loading of Sr and Ca. PC2 and PC3 explains around 10% of variance each. PC2 has a strong negative loading of Fe contrasting with the positive loading of all other elements, with a weak loading of Ti, Rb, and Zr (Fig. 7). PC3 has its positive pole primarily driven by K, Si, Zr, Sr and Ca, and less by Rb and Ti. It has a strong negative pole at Al, and Fe to a lower extent.

https://doi.org/10.5194/egusphere-2024-2499
Preprint. Discussion started: 20 August 2024

In PC1, the elements with positive loadings are associated with detrital sediments originating from the continent, while Ca often represents carbonate of marine origin and Sr substitutes for Ca in these carbonates (Govin et al., 2012). Ratios like Fe/K display a comparable pattern with PC1, suggesting that PC1 can be used to represent terrestrial element variability.

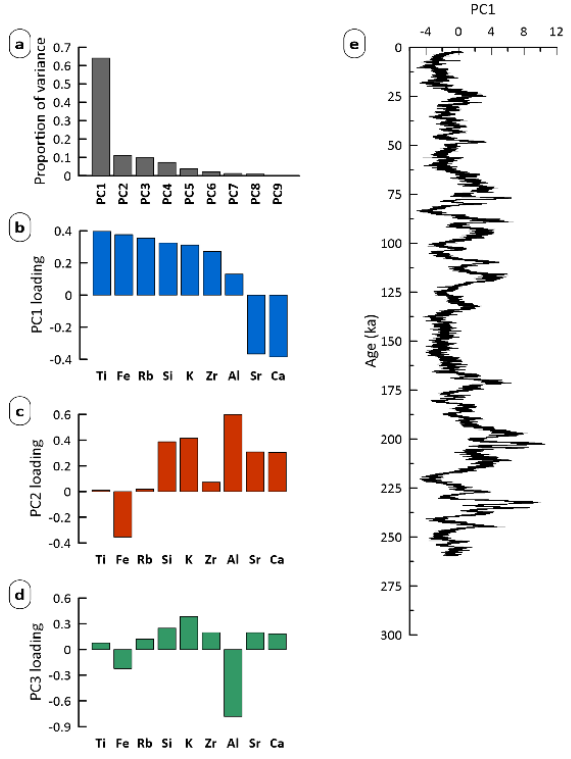

Figure 7. Principal component analysis. (**a)** Explained variance of each principal component. (**b)** Loadings of principal component 1 (PC1) in blue. (**c)** Loadings of principal component 2 (PC2) in red. (**d)** Loadings of principal component 3 (PC3) in green. (**e)** PC1 plotted against depth, in black.

4.4 Spectral analysis

The power spectra identified different frequencies in fig. 8 **a**, notably at 20 ka, 23 ka, 41 ka and 122 ka. All of these are above the 99% significance level and show that changes in the supply of terrigenous elements vs marine elements in the core have cyclicities that coincide with orbital cyclicities associated with precession for the 20 and 23 ka peaks, obliquity for the 42 ka peak, and potentially eccentricity for the 122 ka peak. Measuring the power spectra of eccentricity over the last ~250 ka, with the same methodology that was used for PC1, gives a peak over the 99% confidence level at ~119 ka. This indicates

https://doi.org/10.5194/egusphere-2024-2499
Preprint. Discussion started: 20 August 2024

that the ~122 ka cyclicity observed in PC1 could be linked with eccentricity (see Fig. S1 c). However, the peak found at ~34 ka on PC1 is not as easily explained. Measuring the power spectra of obliquity reveals an additional peak at 34 ka (see Fig. S1 b), which could correspond to the peak observed in PC1.

The orbital parameters can then be compared with the output from applying gaussian filters to PC1 in figure 8 **b**. The 23 ka filter output on PC1 matches well with Earth's precession throughout most of the core, however in the youngest ~75 ka and older than ~175 ka there are notable differences in amplitude. The 41 ka filter output seems out of phase with Earth's obliquity. Starting from the bottom of the core, there is an increased lag of the filter output from obliquity, approaching an anti-phased relationship in the younger half of the core. The 122 ka filter output produces a result that seems similar to Earth's eccentricity, with an offset of the filtered output towards the present in comparison with eccentricity.

The wavelet analysis in figure 8 **c** shows how the dominant cyclicities changed through time. From ~190 ka to ~140 ka the ~41 ka cyclicity (obliquity) is strong, and after ~130 ka the ~23 ka cyclicity (precession) dominates, while the ~122 ka cyclicity is outside the cone of influence. Information outside the cone of influence should be treated with caution because of edge effects: the wavelet analysis assumes the data is cyclic and thus errors will occur at the beginning and end of the wavelet power spectrum since we are using finite-length time series (Torrence, 1998). A longer time series would be necessary to correctly identify this frequency. In summary, these results confirm that the orbital parameters of precession (~23 ka) and obliquity (~41 ka) can indeed be linked with changes in the supply of terrigenous elements into the marine realm of the region. The wavelet analysis implies that prior to ~140 ka, obliquity is the dominant forcing factor, whereas after this time precession dominates. While the gaussian filtered data and the eccentricity looks similar (Figure 8c), it is difficult to confidently assert that eccentricity itself drives the observed signal due to a difference in time scale (~100 ka for eccentricity vs ~122 ka observed in PC1) and a short time series in comparison to the eccentricity time scale (~250 ka vs ~100 ka).

https://doi.org/10.5194/egusphere-2024-2499
Preprint. Discussion started: 20 August 2024

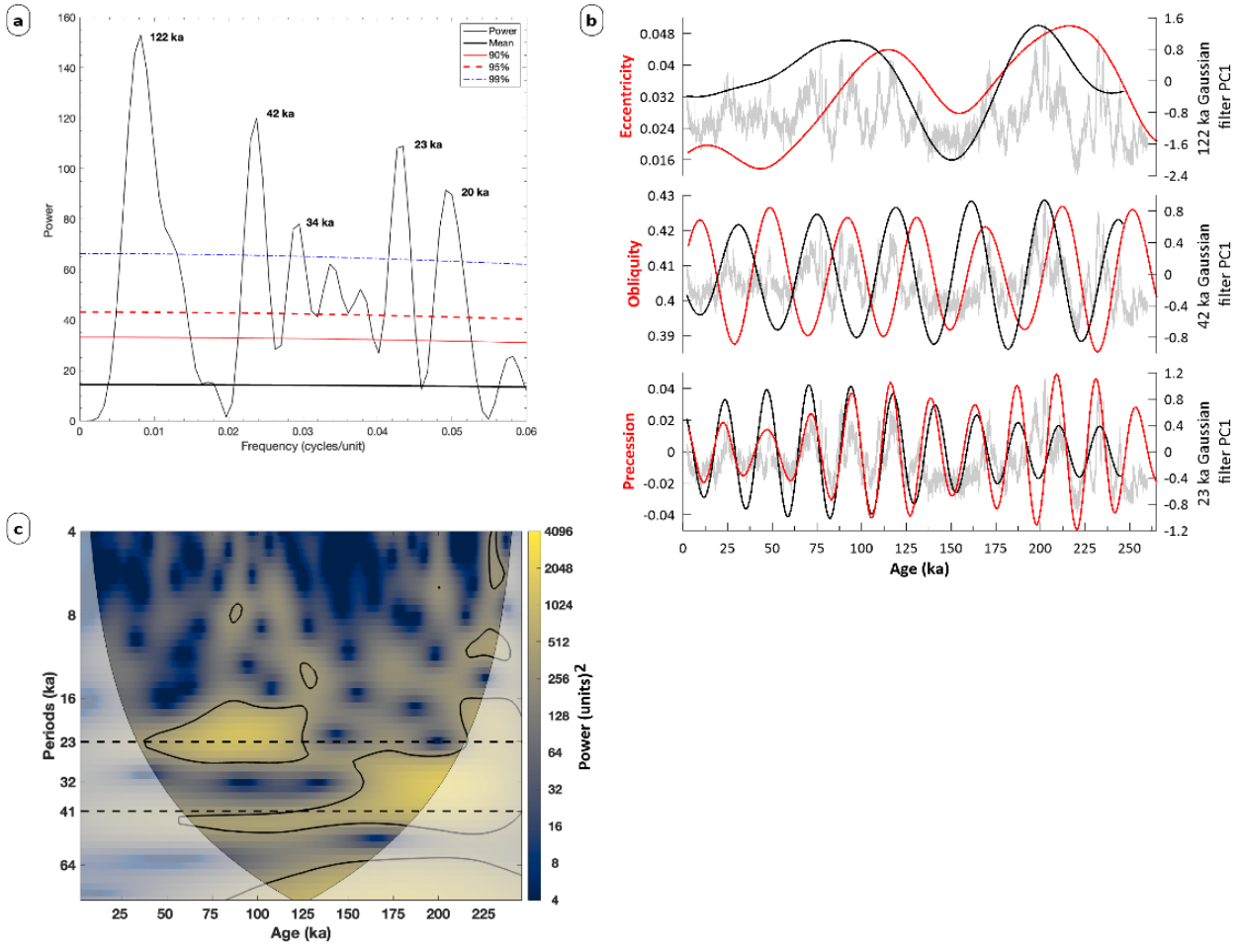

Figure 8. Frequency analysis. (**a**) Power spectrum of PCI on the age model (black). A red noise AR(1) signal is shown (heavy black), and so are the 99% (blue dashed), 95% (red dashed), and 90% (red continuous) confidence levels relative to AR(1). Peaks over the 99% confidence level at 122 ka, 42 ka, and 23 ka are identified. Peaks at ~34 and ~20 ka also appear over the 99% confidence level; see text for explanation. (**b**) Gaussian filters. PC1 is plotted on the age model (grey), while gaussian filters are applied to PC1 with cyclicities of 23, 42, and 122 ka (black). Precession, obliquity, and eccentricity are also shown (red). (**c**) Wavelet transform of PCI on the age model. The morlet wavelet is used as it usually performs best (Hammer et al., 2001). The vertical axis is on a logarithmic scale (base 2). Signal power is shown with colour, while the black contour encircles regions over the 95% confidence level for a red-noise process (Torrence and Compo, 1998). The cone of influence in black shows the regions where boundary effects are present. It can be seen that between ~25 and ~125 ka the cyclicity centred at ~23 ka dominates, while deeper in the core the cyclicity centred at ~41 ka dominates. The 122 ka cyclicity is outside the cone of influence.

https://doi.org/10.5194/egusphere-2024-2499
Preprint. Discussion started: 20 August 2024

5 Discussion

5.1 Orbital timescale climate variability

5.1.1 Interpretation of XRF signal

The similar patterns observed for all ratios in figures 2 and 4, and PC1 in figure 5, imply that similar processes are affecting PC1 and the elemental ratios including Fe/K. High Fe/K is thought to indicate high soil erosion or chemical weathering, pointing to increased precipitation (Govin et al., 2012) in southern South Africa. The type of soil has a notable impact, for instance the Kwa-Zulu Natal province is extensively covered by lixisols, which has a high Fe oxide content, while the eastern Cape and western Cape have a high proportion of luvisols which is lower in Fe oxide, and durisols and leptosols that are even lower in Fe oxide (Driessen et al., 2001; Garzanti et al., 2014). The relationship between Fe/K and river catchment precipitation can also be affect by other factors, notably vegetation cover, where low cover increases soil erodibility (Ludwig and Probst, 1998), organic acids released by vegetation which can increase the dissolution rate of minerals (Benedetti et al., 1994), high temperatures accelerating chemical weathering in subtropical humid regions (Driessen et al., 2001), and diagenetic Fe remobilisation in marine sediments due to redox processes linked with changes in sedimentation rates or turbidites (e.g., Thomson et al., 1996).

Because the elemental oxide ratios are dependent on variations in the calcium input, i.e. marine productivity and preservation, as well as terrestrial input, i.e. other elements, variations in both need to be considered when making inferences based on these data. A higher amount of CaO originating from increased productivity could be expected during glacial intervals due to the intensification of trade winds and enhanced oceanic upwelling (Hernández-Almeida et al., 2019; Tangunan et al., 2021) and this could affect the interpretation of the XRF data. The pattern in the CaO concentrations from the discrete samples and the calibrated XRF measurements in core MD20-3592 between the LGM and the Holocene does not support this (Fig. S2.). In the two previous glacial-interglacial transitions, there is also no increase in CaO % corresponding to an expected increased productivity during glacial intervals. Changes in deep water masses properties at the coring site can also affect the preservation or dissolution of carbonates. Hines et al. (2021) and Yu et al. (2020) showed that during the LGM, a water mass with a low carbonate ion concentration reached up to 20º S in the South Atlantic at 3-4 km depth. This water mass, named Glacial Pacific Deep Water (GPDW), was enriched in carbon and therefore more corrosive to calcite. Nevertheless, this potentially amplified dissolution during glacials is not evident in core MD20-3592 (Fig. S2.), possibly due to the study site being relatively deeper than the core of the GPDW. Consequently, the ratios of terrestrial elements on calcium are primarily driven by variations in terrestrial element inputs. This in turn implies that the inverse relationship observed between the terrestrial elements and Ca (and Sr) confirm that downcore variations in geochemistry are controlled by changes in terrigenous sediment supply carried by southern African rivers, assuming an approximatively constant or low fluctuations in the flux of marine biogenic sediments containing Ca and Sr.

https://doi.org/10.5194/egusphere-2024-2499
Preprint. Discussion started: 20 August 2024

The sedimentation rate calculated with the radiocarbon dates can give additional information on the processes controlling the sediment supply at core site MD20-3592. During MIS 2, there were significant sedimentation rate changes, with a maximum occurring during the LGM (up to 48 cm/ka). This can be interpreted to be due to increasing sediment supply by the rivers to the core site that increases the sedimentation rate in this interval. This in turn can be the result of two different processes; a) increases of sediment supply from the river catchments to the core location due to more humid conditions on land from either increased summer rains or winter rains, b) migration of river mouths closer to the core site in response to eustatic sea-level change. The latter situation occurs during sea level low-stands such as the LGM when significant coastline shifts in South Africa took place and rivers deltas moved seaward due to the Paleo-Agulhas plain exposure (Cawthra 2020). The maximum sedimentation rate does indeed occur at ~20 ka, shortly after the period of lowest sea level (Fig. S3). This indicates that variations of river mouth locations due to sea-level change probably had an important influence on sedimentation rates, and some of the sediments likely originated from the exposed Agulhas bank. However, processes of increased sediment supply from the catchments occurring simultaneously cannot be ruled out. Climate model results by Engelbrecht et al. (2019) have shown supporting evidence for such a scenario with southern South Africa experiencing a wetter climate during the LGM due to an increase in winter rains.

Another potential source of variability in the elemental composition of the sediments can originate from aeolian dust fluxes. The predominance of easterly winds in this region limits the amount of aeolian deposition at the coring site, since it is located to the south of potential dust sources (e.g., South Africa). Modelled aeolian mass accumulation rates in the study region for the LGM are 4-10 g/m^2/year and 0.5-1 g/m^2/year for the present, with dust coming mainly from the Kalahari Desert region and some from South America (Mahler et al., 2010). Using the mean accumulation rate (16.5 cm/ka) and density (0.88 g/cm^3) of core MD20-3592, these dust fluxes equate to 3-7% (LGM) and 0.3-0.7% (present day) of the core sediment accumulation rate. Nonetheless, sustained periods of low sediment accumulation rates (< 10 cm/ka) occur between 131-113 ka and younger than 4 ka, during which LGM levels of aeolian input would be proportionally more important. However, because these two periods of low sedimentation are centred upon, or solely within interglacials, it is reasonable to assume that approximatively present-day levels of aeolian inputs occurred. On this assumption, the aeolian contribution to sedimentation rates ranges between 0.7-1.3% in these periods. Therefore, dust flux is unlikely to be an important driver of elemental ratios in MD20-3592.

Overall, the lithogenic versus marine carbonate record expressed in PC1 shows a comparable pattern with Fe/K suggesting that high lithogenic input can be associated with increased soil erosion or chemical weathering, which indicates increased riverine sediment discharge, therefore more humid conditions, and in turn (seasonal) increased rainfall.

https://doi.org/10.5194/egusphere-2024-2499
Preprint. Discussion started: 20 August 2024

5.1.2 Orbital timescales

The 122 ka periodicity observed in PC1 can potentially be linked with orbital eccentricity. In figure 8c, it can be seen that the 122 ka gaussian filter lags orbital eccentricity by ~20 ka, with a high PC1 occurring during intervals of high eccentricity such as during MIS 5 and MIS 7. Orbital eccentricity comprises 3 components: 413 ka, 125 ka, and 96 ka (Maslin and Ridgwell, 2005). Eccentricity is the change of the orbit of the Earth around the Sun from circular to more elliptical (Campisano, 2012). A circular orbit means more even insolation throughout the year, while an elliptical orbit means higher (lower) insolation at perihelion (aphelion). This affects seasonality; the more elliptical the more the seasonality will be pronounced in one hemisphere and muted in the other (Maslin and Ridgwell, 2005). It is to be noted that in discussions of orbital eccentricity, it is generally referred to as a 100 ka cycle, and many climate archives do display this cyclicity. However, the length of the PC1 time series is too short to resolve a ~100 ka frequency accurately; Rial (1999) showed that a time window of 600 ka merged all the spectral peaks related to eccentricity and the PC1 time series is less than half of this time window. Despite the caveats mentioned, the fact that the 122 ka gaussian filter applied on PC1 was relatively in phase with the ~100 ka eccentricity cycle suggests this cycle has an influence on the regional climate recorded in core MD20-3592. The higher amplitude of PC1 on the precessional timescale during intervals of higher eccentricity (e.g., MIS 5 and MIS 7) could be then explained by the amplification of seasonality. This amplification either increases or reduces local SH summer insolation when the perihelion coincides with the SH summer or winter, which is determined by precession (see below). In regions where high latitude drivers dominate, as opposed to climatic changes driven by changes in local insolation, changes in climatic sequences with the 100 ka periodicity can more plausibly be linked with the influence of obliquity and precession at high northern latitudes and the development of ice sheets (Chase, 2021). In contrast, in tropical regions, changes with a ~100 ka periodicity can more conceivably be linked with the eccentricity modulating variations in direct insolation (Chase, 2021). The presence of a dominant precessional (~23 ka) signal can provide indication of a low latitude forcing dominance, whereas the absence or muting of a 23 ka signal paired with a significant 41 ka signal indicates the prevalence of high latitude mechanisms (Chase, 2021). In the case of core MD20-3592 where the ~41 ka signal has a high power, as well as ~23 ka and ~122 ka in figure 8a, both high and low latitude forcing appear to be important.

The relationship observed between PC1 and obliquity varies through the core. The PC1 filter (black line; Fig. 8b) lags obliquity (red line: Fig. 8b) by ~10 ka. The matching variation of PC1 in phase with obliquity from the deeper part of the core up to 125 ka could be explained by a stronger cross-equatorial transport of moisture towards the summer hemisphere when obliquity is high (Bosmans et al., 2015; Daniau et al., 2023). Bosmans et al. (2015) observed in model experiments that during obliquity maxima, surface winds towards the summer hemisphere are strengthened, leading to an increase in moisture transport over the Indian Ocean and increased precipitation over part of the southern African summer monsoon region. The strengthened winds can be explained by an enhanced inter-hemispheric pressure gradient, which is itself driven by an increase in the summer inter-tropical insolation gradient (Bosmans et al., 2015). However, from ~125 ka to the present, the

https://doi.org/10.5194/egusphere-2024-2499
Preprint. Discussion started: 20 August 2024

relationship appears antiphased (Fig. 8b). This observation is confirmed with the cross wavelet transform, as indicated by the arrows in fig. S6. The obliquity cycle results from an oscillation in the axial tilt of the Earth, with higher angles of tilt resulting in more extreme seasonal temperature changes (Maslin and Ridgwell, 2005). Obliquity forcing is in-phase between the hemispheres and is more pronounced at high latitudes. Such changes in seasonality may potentially explain the presence of a signal at the obliquity frequency in PC1 either as a result of a direct influence on regional insolation, or through impacts of changes originating at higher latitudes. However, the lack of a consistent phase relationship between the gaussian filter and obliquity hinders attempts to infer a causal relationship between obliquity and the regional hydroclimate recorded in core MD20-3592.

The precession signal is significant throughout the majority of the core as indicated by the frequency analysis (figure 8a), however it appears to have the strongest influence between ~140 ka and ~40 ka (figure 8c). Precession affects the distribution of solar insolation during the seasons, with an inverse relationship between the hemispheres. Local summer insolation is tightly coupled with the precession index (Fig. S5), with high local insolation coinciding with a high precession index. Indeed, Singarayer and Burrough (2015) found based on modelling experiments that the austral summer rainbelt moves southward during periods of increased local summer insolation. This is confirmed by proxy data that found that in southwestern Africa, increased local insolation is linked with an extension of the range or an intensifying of tropical systems that bring summer rainfall to this region (Chase, 2021). Most summer rains over South Africa come from synoptic scale tropical-temperate through (TTT) systems (Todd et al., 2004). During these events tropical convection over Africa is coupled with mid-latitude transient systems and brings a band of clouds and high rainfall that extends from central Africa south-eastwards, and is associated with the ITCZ (Todd et al., 2004). The tropical systems that are part of the TTT are weather systems driven by high SST and warming of the continents during the summer to establish strong convection cells (Chase and Meadows, 2007). Periods of high local summer insolation due to a high precession index could thus increase the summer precipitation in the YRZ by providing more energy to the tropical systems via increased SST and continental warming. In short, PC1 in core MD20-3592 displays a strong 23 ka cyclicity which matches with orbital precession, and this finding gives additional support to the idea that precession is a major driver for precipitation in this region.

5.2 Wider regional comparison

In Fig. 9 and 10, the XRF-derived PC1 of core MD20-3592 is compared to regional climate archives helping to understand the importance of the different climatic drivers, and potential shifts in the dominant forcing factors. Fig. 9 displays records from eastern and southern South Africa, while Fig. 10 shows records from western South Africa. Both figures include the LR04 $\delta^{18}O$ global benthic stack and the EDC ice core δD record, in order to allow the comparison of these reference records with the South African regional climate archives.

https://doi.org/10.5194/egusphere-2024-2499
Preprint. Discussion started: 20 August 2024

For the Cango Caves (Fig. 9 (c)), a composite speleothem record named "Cape Fold composite" was produced by Chase et al. (2021). This record appears to match mostly with MD20-3592 PC1 in the intervals between MIS 5 to the present. High $\delta^{13}C$ values in that record correspond to increased C4 grass abundance and increased summer rains. Hence high summer rainfall is inferred for both these records between ~98 and ~88 ka, between ~77 and ~65 ka, a peak at ~25 ka, and increasing summer rains during the Holocene. This pattern is reflected in the MD20-3592 XRF PC1 record with higher values indicating more terrigenous sediment supply. However, core site MD20-3592, which records regional river catchments extending further inland than the Cango Caves site (see Fig. 1), is likely to be less affected by shifts in sea level and climate over the ocean than the Cango Cave speleothem record. This can be seen with the larger amplitude variations in MD20-3592 on precessional timescale in MIS 2 and 3 in comparison with the speleothem record, the latter displaying indications of generally lower precipitation during sea level low stands from MIS 4 to MIS 2. This interpretation of a more arid climate at the Cango Caves linked with a lower sea level is supported by leaf wax $\delta^{2}H$ values from nearby Blombos Cave, and modelling results over coastal southern Africa (Göktürk et al., 2023). The modelling from this aforementioned study indicates that in MIS 4 ka at coastal sites in this region, the lower sea level reduced the precipitation year-round by increasing the continentality of the sites, and this could explain the reduction in summer rainfall in the Cango Caves. These caves are currently within the coastal zone (100 km from the ocean; Brown, 2006) which receives a strong influence from the ocean, and this is not the case for major portions of the river catchments providing the sediments to the study core.

Along the eastern coast of South Africa, the XRF derived Fe/K record of CD154-10-06P (Fig. 9 (d); Simon et al., 2015) displays variations on a precessional timescale that correspond well with core MD20-3592, with some differences in MIS 2 and MIS 6. Marine core site CD154-10-06P integrates the signal from a wide area in the KwaZulu-Natal province, adjacent to the Eastern Cape province which is likely a major source of sediments in core MD20-3592. The similarity between these two sequences implies that they share the same dominant climate forcings. Results produced by numerical modelling in Simon et al. (2015) indicated that in eastern South Africa, increased precipitation during precession maxima is mainly driven by higher insolation heating up the continent more than the ocean. This causes the development of lower pressure over the continent, which drives moisture from the Indian Ocean and the Mozambique coast towards the KwaZulu-Natal and the Eastern Cape province.

Core MD96-2048 (Fig. 9 (e); Caley et al., 2018) receives sediments from the Limpopo River catchment. Similar patterns in the Fe/Ca ratio of this core in comparison with the study core are observed in MIS 1, 2, 5 and 7. This similarity can be explained by a statistically significant amount of precessional forcing component identified in the Limpopo core. Caley et al. (2018) explains the influence of precession on the local precipitation with higher insolation that causes higher temperatures and lower surface pressure, especially over land. The contrast between land and ocean strengthens moisture inflow from the Indian Ocean towards southeastern Africa, increasing rainfall. However, there are differences between the study core and

https://doi.org/10.5194/egusphere-2024-2499
Preprint. Discussion started: 20 August 2024

MD96-2048, in particular during MIS 3, 4, and 6; core MD96-2048 does not have the peaks in precipitations at ~ 50 ka, ~ 72 ka, and ~ 166 ka that are observed in core MD20-3592.

Fig. 9 (f) shows the comparison between core MD20-3592 and the Tswaing crater precipitation record (Patridge et al., 1997). It can be seen that on precessional timescales, increased summer precipitation in southern South Africa during SH summer insolation maxima is in agreement with this record, particularly from MIS 5 to the present. This record is located far inland in northeastern South Africa and is based on soil sediment texture. In comparison with the Limpopo record, this record integrates the signal from a much smaller area. While the Twaing crater follows closely local insolation during most of the record (Partridge et al., 1997), during MIS 2 this relationship is not found and at the end of MIS 6 the peak in precipitation is lower than the peaks before and after. Engelbrecht et al. (2019) projected lower winter rains in this area during MIS 2, plausibly due to lower heat convection and rainfall caused by lower surface temperatures.

Shifting the focus to southwestern South Africa in Fig. 10, core IODP U1479 has been studied for *Podocarpaceae* pollen which are used as an indicator of Afrotemperate forests, which require at least 525 mm of annual rainfall (Fig. 10 (c); Dupont et al., 2022). The pattern observed in this record is very similar to the XRF PC1 record from MD20-3992 from MIS 5 to the present, similar in MIS 8 and 7 but with some major differences in MIS 6. A common feature between the records in MIS 6 is drier conditions on average during this period. Dupont et al. (2022) interpret their pollen record as indicating increasing summer rains during phases of maximum precession and local summer insolation, which is consistent with the main interpretation for the study core.

Northwestward of the previous record, off the Namibian coast, the δD of n-C_{31} alkane in leaf waxes from core MD08-3167 shows a dominant precessional component with higher precipitation during precession maxima as observed in the study site (Fig. 10 (d)). Collins et al. (2014) thus conclude that the main driver in hydroclimate of southwestern Africa is precessional insolation variability. However, these findings are in contrast with terrestrial paleoenvironmental evidence from the Namib Desert which indicate that humidity in this region is generally negatively related to summer insolation (Chase, 2019). The apparent discrepancy between marine archives and terrestrial records from the region may arise from either: (1) regional differences in climate signals, where marine records are mainly influenced by sediments originating from central southern Africa, as proposed by Collins et al. (2014) and Daniau et al. (2013), or (2) the influence of aeolian transport shaping the unique variability patterns seen in the marine records.

Further northwest, core MD96-2094 exhibits patterns that are not consistent with those in the study core, with a large portion appearing antiphased (Fig. 10 (e); Stuut et al., 2002). The proportion of aeolian dust in core MD96-2094 is interpreted as indicating continental aridity, with high values indicating increased aridity. Stuut et al. (2002) concludes there is a

https://doi.org/10.5194/egusphere-2024-2499
Preprint. Discussion started: 20 August 2024

predominant influence of the winter rains associated with the SHW in core MD96-2094. However, in nearby core MD08-3167 Collins et al. (2014) excluded this possibility on the basis that there are no shifts in vegetation types indicated by $\delta^{13}C$ and no indication of increased precipitation sourced from the Atlantic. Some of the discrepancy could be explained by the proportion of aeolian dust in MD96-2094 being largely affected by the strength of the trade winds during glacial periods, and to some extent by changes in the dilution effect of sediments coming from marine productivity.

In summary, for eastern and southern South Africa, all records exhibited a strong precession signal, supporting the notion that the precipitation over the river catchments near core MD20-3592 are mainly driven by precession on orbital timescales. However, a strong influence of sea level can be observed in coastal sites such as Cango Caves, which can be explained by their proximity to the ocean. Differences between MD20-3592 and the other cores in eastern and southern South Africa are observed during MIS 6, and could potentially be due to a stronger influence of obliquity on core MD20-3592 in that time period. For the marine cores located west of the study core, the comparisons with the study core give more heterogenous results. Core IODP U1479 displays a very similar pattern with core MD20-3592, pointing again to precession controlling summer rainfall over the region. Core MD08-3167 also has a strong precessional component suggesting that precession controls the hydroclimate in southwestern Africa. Core MD96-2094 exhibits noticeably different patterns from the study core, which could be explained by a strong influence of the winter rains, but also by changes in the strength of the trade winds affecting the proxy record.

Increased rains during precession maxima can indicate that the proportion of summer rain increases, however the contribution of the winter rainfall has to be examined. Climate model results from Engelbrecht et al. (2019) projected that during the LGM the winter season was drier at the Cape south coast but wetter inland. Conditions were projected to be more humid inland due to frontal systems making landfall at more northerly locations than present, caused by an equatorward shift in the SH westerlies (Engelbrecht et al., 2019). This equatorward displacement is thought to result from an enhanced meridional temperature gradient, and additional factors contributing to this shift are the expansion of the polar high pressure cells and sea-ice (Engelbrecht et al., 2019). The model results project an expansion of the YRZ in the current SRZ. Conversely, rainfall decreases were projected near the coast because of a rain shadow occurring southeast of the Cape Fold mountains, with hot and dry berg-winds being induced (Engelbrecht et al., 2019). According to these results, there would have been uneven effects in the river catchments feeding the sediments to the study coring site: in winter the upper catchments would have received more rain while the lower catchments would have received less. Additionally, work by Miller et al. (2020) and Hahn et al. (2021b) suggests that an equatorward displacement of the SHW due to increase in sea ice that occurred during the MIS 1 and MIS 5 was associated with a north-eastward displacement of the SIOCZ and its associated rainfall. This mechanism could also have been present during glacial periods and could have reduced summer rainfalls over the south Cape coast, which seems to be the case during MIS 8, MIS 6 and MIS 3 in the study core and the Cape Floristic core IODP U1479 (Fig. 10). Additionally, both of these cores would have had the projected increase in winter

https://doi.org/10.5194/egusphere-2024-2499
Preprint. Discussion started: 20 August 2024

rains inland mitigated by the decreased winter rains south and east of the Cape Fold mountains. Sites located northeast of the study site (Fig. 1, Fig. 9 d-f) do not exhibit this pattern, and this could be explained by these sites still remaining under the summer precipitation brought by the SIOCZ displaced towards the equator. However, it is to be noted that there are alternative scenarios that can explain wetter conditions in southwestern South Africa during glacial periods such as the LGM, where the westerlies are shifted poleward or weakened (Mcgee, 2020; Sime et al., 2013)

Finally, the data from core MD20-3592 can be used to provide a climatic context for the ~ 120-50 ka time interval during which evidence of behavioural complexity in humans appears in South Africa. The general climatic trends inferred from the MD20-3592 PC1 record are as follows: 1) Initial humid conditions at ~120 ka become progressively more arid from ~117 to ~102 ka; 2) More humid conditions return between ~98 and 88 ka, after which a pronounced period of aridity centred on ~83 ka occurs; 3) Conditions become progressively more humid between ~ 83 and ~72 ka, after which progressive aridification occurs until ~60 ka; 4) Arid conditions persist until ~50 ka.

https://doi.org/10.5194/egusphere-2024-2499
Preprint. Discussion started: 20 August 2024

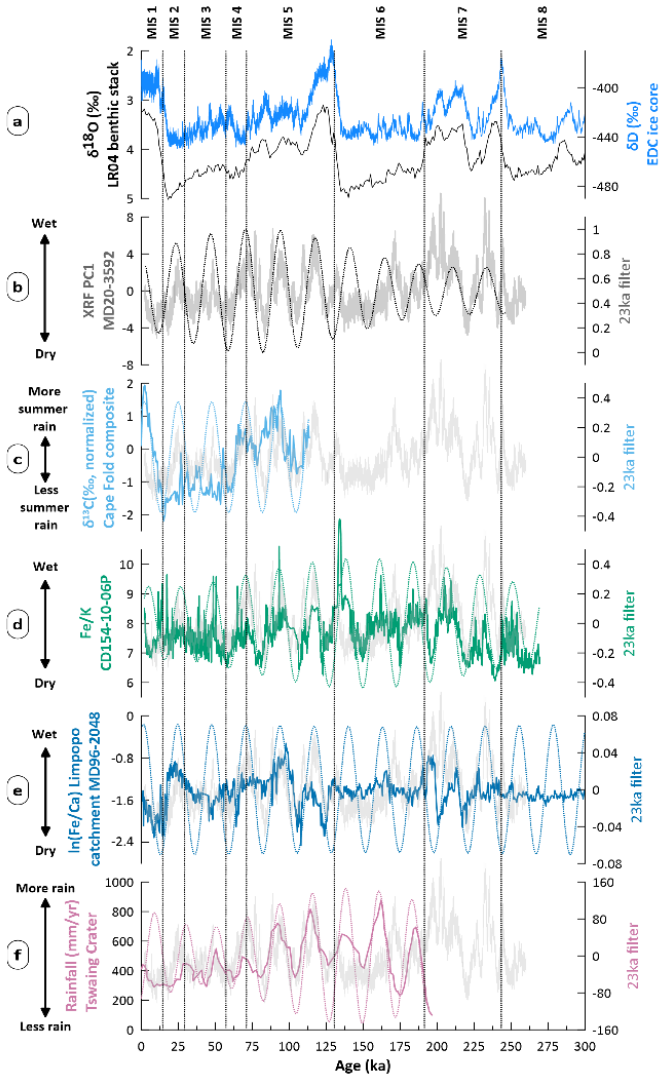

Figure 9. Comparison with global, local and eastern south African records. (**a**) Global records: LR04 $\delta^{18}O$ global benthic stack (Lisiecki and Raymo, 2005), and EDC δD record on the AICC2012 chronology (Bazin et al., 2013; Veres et al., 2013). (**b**) PC1 of XRF in core MD20-3592. (**c**) $\delta^{13}C$ Cape Fold composite record (Chase et al., 2021). (**d**) Fe/K of core CD154-10-06 P (Simon et al., 2015). (**e**) ln(Fe/Ca) of core MD96-2048 (Caley et al., 2018). (**f**) annual rainfall at Tswaing Crater (Partridge et al., 1997). Dotted lines are a 23 ka Gaussian filter applied on each time series. Core MD20-3592 PC1 data is superimposed on each time series, in light grey. Marine isotopes stages (MIS) 1 to 8 (Lisiecki and Raymo, 2005) are labelled.

https://doi.org/10.5194/egusphere-2024-2499
Preprint. Discussion started: 20 August 2024

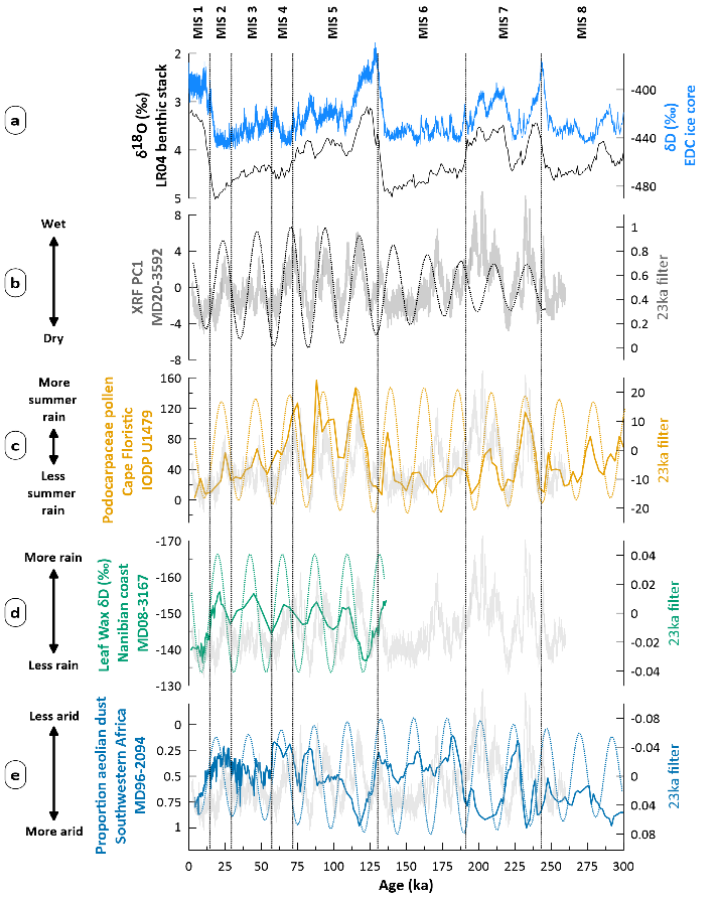

Figure 10. Comparison with western south African records. (**a**) Global records: LR04 $\delta^{18}O$ global benthic stack (Lisiecki and Raymo, 2005), and EDC δD record on the AICC2012 chronology (Bazin et al., 2013; Veres et al., 2013). (**b**) PC1 of XRF in core MD20-3592. (**c**) Podocarpaceae pollen in core IODP U1479. (**d**) Leaf wax δD in core MD08-3167. (**e**) Proportion of aeolian dust in core MD96-2094. Dotted lines are a 23 ka Gaussian filter applied on each time series. Core MD20-3592 PC1 data is superimposed on each time series, in light grey.

6 Conclusions

Core MD20-3592 is the first marine sediment core off the coast of southern South Africa which allows for a reconstruction of the climatic conditions over the past two glacial cycles. We produced an XRF core scanning record of elemental composition for this core and made available calibrations to obtain quantitative ratios of the elemental compositions. Comparison to nearby paleoclimate archives (Simon et al., 2015; Chase et al., 2021) suggests that the climate signal in

https://doi.org/10.5194/egusphere-2024-2499
Preprint. Discussion started: 20 August 2024

MD20-3592 represents the hydroclimatic variations experienced by southern South Africa river basins, and sediment provenance studies of the area have indicated that a major portion of the lithogenic sediments at the core site are from local sources inland (Franzese et al., 2009).

Variations in the proportion of elements of terrestrial origin compared to marine carbonates in the core are interpreted to be controlled by changes lithogenic input, with enhanced terrestrial inputs due to increased fluvial discharge during humid periods. Variations in terrestrial inputs have periodicities which imply orbital forcing of climate change. One of the main frequencies observed throughout most of the core is a precessional (~23 ka) signal. This is a common feature in South African sequences and can be explained by the local insolation being mostly affected by orbital precession. Periods of high local summer insolation caused by a high precession index are thought to increase the summer precipitation over the YRZ by warming the continent faster than the ocean in summer and establishing a stronger convection cell. This is in line with modelling work which showed an increased flow of moist air from the Indian Ocean and the coast of Mozambique towards eastern South Africa (Simon et al., 2015)

An obliquity (~42 ka) signal was also detected in the PC1 time series, lagging behind orbital obliquity from the bottom of the core until ~125 ka and then exhibiting an antiphase relationship from 125 ka until the present. The inconsistent phasing makes it difficult to explain a mechanistic relationship between obliquity and the signal observed in MD20-3592. Finally, a ~122 ka cyclicity was observed in the core, which could be tied to orbital eccentricity. This observation could be explained by eccentricity modulating precession amplitude, since higher eccentricity causes higher precession and can therefore increase summer precipitation.

Lower precipitation during MIS 3, 6 and 8 observed in the study core and the Cape Floristic core IODP U1479 could be explained by a northward shift of the SIOCZ and its related precipitation, in response to an equatorward shift in the SHW during glacial periods. This shift of the SHW would have brought more winter rains to southwestern South Africa, however drier conditions would have been experienced at the Cape south coast due to a rain shadow effect east and south of the Cape Fold mountains. However, other mechanisms have been proposed for the observed wetter conditions in southwestern South Africa and drier conditions towards the east during the LGM (Mcgee, 2020; Sime et al., 2013).

Lastly, the data from core MD20-3592 can be used to provide a climatic context for the ~ 120-50 ka time interval during which evidence of behavioural complexity appears in South Africa. Several successive technocomplexes took place in southern South Africa during that time interval, notably the Still Bay (76-71 ka) and Howiesons Poort 66-59 ka (Lombard et al., 2012; d'Errico et al., 2017). During this watershed period for human behavioural evolution, our PC1 record chronicles large amplitude oscillations of precipitation on a precessional timescale. The general climatic trends inferred from the record are as follows: 1) Initial humid conditions at ~120 ka became progressively more arid from ~117 to ~102 ka; 2) More humid

https://doi.org/10.5194/egusphere-2024-2499
Preprint. Discussion started: 20 August 2024

conditions returned between ~98 and 88 ka, after which a pronounced period of aridity centred on ~83 ka occurs; 3) Conditions became progressively more humid between ~ 83 and ~72 ka, after which progressive aridification occurred until ~60 ka; 4) Arid conditions persist until ~50 ka.

720

Data availability. All results from this study are available in the Supplement to this publication.

Supplement. The supplementary material related to this article is available
725 online at: https://doi.org/.....

Author contributions. Study design: KP, MHS, EJ, SA; methodology and data acquisition: KP, MHS, EP, JVDL; visualization and original draft preparation: KP; writing and editing: KP, MHS, EJ, SA, EP.

730 **Competing interests.** The contact author has declared that none of the authors has any competing interests.

Disclaimer. Publisher's note: Copernicus Publications remains neutral with regard to jurisdictional claims in published maps and
735 institutional affiliations.

Acknowledgements. We thank Natalia Vazquez Riveiros, Claire Waelbroeck, the captain, officers and crew of RV Marion Dufresne Cruise No. MD20-225. Sub sampling of the sediment core was conducted by Dag Inge Blindheim at NORCE in Bergen. Siv Hjorth Dundas and Hildegunn Almelid were responsible for element and trace element analysis at Universitetet I
740 Bergen. Eivind Støren oversaw XRF analysis, with the help of Sunniva Rutledal and Alan Kvindesland at Universitetet I Bergen. Oxygen isotope analysis was conducted under the supervision of Ulysses Silas Ninnemann at Universitetet I Bergen. The AMS measurements for ^{14}C were made conducted at at ETH Zurich.

Financial support. This research has been supported by the Research Council of Norway, through its Centres of Excellence
745 funding scheme, SFF Centre for Early Sapiens Behaviour (SapienCE), project number 262618.

https://doi.org/10.5194/egusphere-2024-2499
Preprint. Discussion started: 20 August 2024

References

Bar-Matthews, M., Marean, C. W., Jacobs, Z., Karkanas, P., Fisher, E. C., Herries, A. I. R., Brown, K., Williams, H. M., Bernatchez, J., Ayalon, A., and Nilssen, P. J.: A high resolution and continuous isotopic speleothem record of paleoclimate and paleoenvironment from 90 to 53 ka from Pinnacle Point on the south coast of South Africa, Quaternary Sci. Rev., 29, 2131–2145, https://doi.org/10.1016/j.quascirev.2010.05.009, 2010.

Bazin, L., Landais, A., Lemieux-Dudon, B., Toyé Mahamadou Kele, H., Veres, D., Parrenin, F., Martinerie, P., Ritz, C., Capron, E., Lipenkov, V., Loutre, M. F., Raynaud, D., Vinther, B., Svensson, A., Rasmussen, S. O., Severi, M., Blunier, T., Leuenberger, M., Fischer, H., Masson-Delmotte, V., Chappellaz, J., and Wolff, E.: An optimized multi-proxy, multi-site Antarctic ice and gas orbital chronology (AICC2012): 120-800 ka, Clim. Past, 9, 1715–1731, https://doi.org/10.5194/cp-9-1715-2013, 2013.

Benedetti, M.F., Menard, O., Noack, Y., Carvalho, A. and Nahon, D.: Water-rock interactions in tropical catchments: field rates of weathering and biomass impact, Chem. Geol., 118(1-4), 203-220, https://doi.org/10.1016/0009-2541(94)90177-5, 1994.

Beyin, A., Wright, D. K., Wilkins, J., and Olszewski, D.I. (Eds): Handbook of Pleistocene Archaeology of Africa, Springer, https://doi.org/10.1007/978-3-031-20290-2, 2023.

Bosmans, J. H. C., Hilgen, F. J., Tuenter, E., and Lourens, L. J.: Obliquity forcing of low-latitude climate, Clim. Past, 11, 1335–1346, https://doi.org/10.5194/cp-11-1335-2015, 2015.

Bradfield, J., Lombard, M., Reynard, J., and Wurz, S.: Further evidence for bow hunting and its implications more than 60 000 years ago: Results of a use-trace analysis of the bone point from Klasies River Main site, South Africa, Quaternary Sci. Rev., 236, https://doi.org/10.1016/j.quascirev.2020.106295, 2020.

Braun, K., Bar-Matthews, M., Matthews, A., Ayalon, A., Zilberman, T., Cowling, R. M., Fisher, E. C., Herries, A. I. R., Brink, J. S., and Marean, C. W.: Comparison of climate and environment on the edge of the Palaeo-Agulhas Plain to the Little Karoo (South Africa) in Marine Isotope Stages 5–3 as indicated by speleothems, Quaternary Sci. Rev., 235, https://doi.org/10.1016/j.quascirev.2019.06.025, 2020.

Brown, C., Corcoran, E., Herkenrath, P., Thonell, J. (Eds.): Marine and coastal ecosystems and human wellbeing: A synthesis report based on the findings of the Millennium Ecosystem Assessment, United Nations Environment Programme (UNEP), 76 pp., https://www.unep.org/resources/report/marine-and-coastal-ecosystems-and-human-well-being-synthesis-report-based-findings, 2006.

Brown, K. S., Marean, C. W., Herries, A. I. R., Jacobs, Z., Tribolo, C., Braun, D., Roberts, D. L., Meyer, M. C., and Bernatchez, J.: Fire as an engineering tool of early modern humans, Science, 325, 859–862, https://doi.org/10.1126/science.1175028, 2009.

https://doi.org/10.5194/egusphere-2024-2499
Preprint. Discussion started: 20 August 2024

Caley, T., Extier, T., Collins, J. A., Schefuß, E., Dupont, L., Malaizé, B., Rossignol, L., Souron, A., McClymont, E. L., Jimenez-Espejo, F. J., García-Comas, C., Eynaud, F., Martinez, P., Roche, D. M., Jorry, S. J., Charlier, K., Wary, M., Gourves, P. Y., Billy, I., and Giraudeau, J.: A two-million-year-long hydroclimatic context for hominin evolution in southeastern Africa, Nature, 560, 76–79, https://doi.org/10.1038/s41586-018-0309-6, 2018.

Campisano, C. J.: Milankovitch Cycles, Paleoclimatic Change, and Hominin Evolution, Nature Education Knowledge, 3, 5, 2012.

Cawthra, H. C., Cowling, R. M., Andò, S., and Marean, C. W.: Geological and soil maps of the Palaeo-Agulhas Plain for the Last Glacial Maximum, Quaternary Sci. Rev., 235, https://doi.org/10.1016/j.quascirev.2019.07.040, 2020.

Chase, B. M.: Orbital forcing in southern Africa: Towards a conceptual model for predicting deep time environmental change from an incomplete proxy record, Quaternary Sci. Rev., 265, https://doi.org/10.1016/j.quascirev.2021.107050, 2021.

Chase, B. M. and Meadows, M. E.: Late Quaternary dynamics of southern Africa's winter rainfall zone, Earth-Science Rev., 84, 103–138, https://doi.org/10.1016/j.earscirev.2007.06.002, 2007.

Chase, B. M. and Quick, L. J.: Influence of Agulhas forcing of Holocene climate change in South Africa's southern Cape, Quaternary Res. (United States), 90, 303–309, https://doi.org/10.1017/qua.2018.57, 2018.

Chase, B.M., Niedermeyer, E.M., Boom, A., Carr, A.S., Chevalier, M., He, F., Meadows, M.E., Ogle, N. and Reimer, P.J.: Orbital controls on Namib Desert hydroclimate over the past 50,000 years, Geology, 47(9), 867-871, https://doi.org/10.1130/G46334.1, 2019.

Chase, B., Harris, C., deWit, M. J., Kramers, J., Doel, S., and Stankiewicz, J.: South African speleothems reveal influence of high and lowlatitude forcing over the past 113.5 k.y., Geology, 49, 1353–1357, https://doi.org/10.1130/G49323.1, 2021.

Collins, J. A., Schefuß, E., Govin, A., Mulitza, S., and Tiedemann, R.: Insolation and glacial-interglacial control on southwestern African hydroclimate over the past 140000 years, Earth Planet. Sc. Lett., 398, 1–10, https://doi.org/10.1016/j.epsl.2014.04.034, 2014.

Cook, K. H.: The South Indian convergence zone and interannual rainfall variability over Southern Africa, J. Climate, 13(21), 3789–3804, https://doi.org/10.1175/1520-0442(2000)013<3789:TSICZA>2.0.CO;2, 2000.

Cowling, R. M.: The occurrence of 3 Carbon and 4 Carbon pathways in Fynbos and allied shrublands in the Southeastern Cape South Africa, Oecologia, 58, 121–127, 1983.

Croudace, I. W., Rindby, A., and Rothwell, R. G.: ITRAX: Description and evaluation of a new multi-function X-ray core scanner, Geol. Soc. Spec. Publ., 267, 51–63, https://doi.org/10.1144/GSL.SP.2006.267.01.04, 2006.

Daniau, A. L., Loutre, M. F., Swingedouw, D., Laepple, T., Bassinot, F., Malaizé, B., Kageyama, M., Charlier, K., and Carfantan, H.: Precession and obliquity forcing of the South African monsoon revealed by sub-tropical fires, Quaternary Sci. Rev., 310, https://doi.org/10.1016/j.quascirev.2023.108128, 2023.

Davies, S. J., Lamb, H. F., and Roberts, S. J.: Micro-XRF Core Scanning in Palaeolimnology: Recent Developments, Micro-XRF Studies of Sediment Cores: Applications of a non-destructive tool for the environmental sciences, edited by: Croudace, I.W., and Rothwell R.G., Springer, 189–226, https://doi.org/10.1007/978-94-017-9849-5_7, 2015.

https://doi.org/10.5194/egusphere-2024-2499
Preprint. Discussion started: 20 August 2024

Deacon, H. J.: Late Pleistocene palaeoecology and archaeology in the southern Cape, South Africa, in: The human revolution: behavioural and biological perspectives on the origins of modern humans, edited by: Mellars, P. & Stringer, C. B., Edinburgh University Press, Edinburgh, 547-564, 978-0691085395, 1989.

Demenocal, P.B., Ruddiman, W.F. and Pokras, E.M.: Influences of high-and low-latitude processes on African terrestrial climate: Pleistocene eolian records from equatorial Atlantic Ocean Drilling Program site 663, Paleoceanography, 8(2), 209-242, https://doi.org/10.1029/93PA02688, 1993.

d'Errico, F. and Henshilwood, C. S.: Additional evidence for bone technology in the southern African Middle Stone Age, J. Hum. Evol., 52, 142–163, https://doi.org/10.1016/j.jhevol.2006.08.003, 2007.

d'Errico, F., Banks, W. E., Warren, D. L., Sgubin, G., Van Niekerk, K., Henshilwood, C., Daniau, A. L., and Sánchez Goñi, M. F.: Identifying early modern human ecological niche expansions and associated cultural dynamics in the South African Middle Stone Age, P. Natl. Acad. Sci. USA., 114, 7869–7876, https://doi.org/10.1073/pnas.1620752114, 2017.

Driessen, P., Deckers, J., Spaargaren, O. and Nachtergaele, F. (Eds.): Lecture notes on the major soils of the world, Food and Agriculture Organization of the United Nations (FAO), https://www.fao.org/3/Y1899E/Y1899E00.htm, 2001.

Dunlea, A. G., Murray, R. W., Tada, R., Alvarez-Zarikian, C. A., Anderson, C. H., Gilli, A., Giosan, L., Gorgas, T., Hennekam, R., Irino, T., Murayama, M., Peterson, L. C., Reichart, G. J., Seki, A., Zheng, H., and Ziegler, M.: Intercomparison of XRF Core Scanning Results From Seven Labs and Approaches to Practical Calibration, Geochem. Geophy. Geosy., 21, https://doi.org/10.1029/2020GC009248, 2020.

Dupont, L. M., Zhao, X., Charles, C., Faith, J. T., and Braun, D.: Continuous vegetation record of the Greater Cape Floristic Region (South Africa) covering the past 300000 years (IODP U1479), Clim. Past, 18, 1–21, https://doi.org/10.5194/cp-18-1-2022, 2022.

Engelbrecht, F. A., Marean, C. W., Cowling, R. M., Engelbrecht, C. J., Neumann, F. H., Scott, L., Nkoana, R., O'Neal, D., Fisher, E., Shook, E., Franklin, J., Thatcher, M., McGregor, J. L., Van der Merwe, J., Dedekind, Z., and Difford, M.: Downscaling Last Glacial Maximum climate over southern Africa, Quaternary Sci. Rev., 226, 105879, https://doi.org/10.1016/j.quascirev.2019.105879, 2019.

Franzese, A.M., Hemming, S.R., Goldstein, S.L. and Anderson, R.F.: Reduced Agulhas Leakage during the Last Glacial Maximum inferred from an integrated provenance and flux study. Earth Planet. Sc. Lett., 250(1-2), pp.72-88, https://doi.org/10.1016/j.epsl.2006.07.002, 2006.

Franzese, A. M., Hemming, S. R., and Goldstein, S. L.: Use of strontium isotopes in detrital sediments to constrain the glacial position of the agulhas retroflection, Paleoceanography, 24, 1–12, https://doi.org/10.1029/2008PA001706, 2009.

Garzanti, E., Padoan, M., Setti, M., López-Galindo, A., and Villa, I. M.: Provenance versus weathering control on the composition of tropical river mud (southern Africa), Chem. Geol., 366, 61–74, https://doi.org/10.1016/j.chemgeo.2013.12.016, 2014.

Göktürk, O. M., Simon, M. H., Sobolowski, S. P., Zhang, Z., Van Der Bilt, W., Mørkved, P. T., D'Andrea, W. J., van Niekerk, K. L., Henshilwood, C. S., Armitage, S. J., and Jansen, E.: Behaviourally modern humans in coastal southern

Africa experienced an increasingly continental climate during the transition from Marine Isotope Stage 5 to 4, Front. Earth Sci., 11, 1–20, https://doi.org/10.3389/feart.2023.1198068, 2023.

Govin, A., Holzwarth, U., Heslop, D., Ford Keeling, L., Zabel, M., Mulitza, S., Collins, J. A., and Chiessi, C. M.: Distribution of major elements in Atlantic surface sediments (36°N-49°S): Imprint of terrigenous input and continental weathering, Geochem. Geophy. Geosy., 13, 1–23, https://doi.org/10.1029/2011GC003785, 2012.

Grinsted, A., Moore, J. C., and Jevrejeva, S.: Application of the cross wavelet transform and wavelet coherence to geophysical time series, Nonlinear Proc. Geoph., 11, 561–566, https://doi.org/10.5194/npg-11-561-2004, 2004.

Hahn, A., Neumann, F. H., Miller, C., Finch, J., Frankland, T., Cawthra, H. C., Schefuß, E., and Zabel, M.: Mid-to Late Holocene climatic and anthropogenic influences in Mpondoland, South Africa, Quaternary Sci. Rev., 261, 106938, https://doi.org/10.1016/j.quascirev.2021.106938, 2021a.

Hahn, A., Schefuß, E., Groeneveld, J., Miller, C., and Zabel, M.: Glacial to interglacial climate variability in the southeastern African subtropics (25-20°S), Clim. Past, 17, 345–360, https://doi.org/10.5194/cp-17-345-2021, 2021b.

Hammer, Ø., Harper, D. A. T., and Ryan, P. D.: PAST: PALEONTOLOGICAL STATISTICS SOFTWARE PACKAGE FOR EDUCATION AND DATA ANALYSIS, Palaeontol. Electron., 4(1), 1-9, 2001.

Heaton, T. J., Köhler, P., Butzin, M., Bard, E., Reimer, R. W., Austin, W. E. N., Bronk Ramsey, C., Grootes, P. M., Hughen, K. A., Kromer, B., Reimer, P. J., Adkins, J., Burke, A., Cook, M. S., Olsen, J., and Skinner, L. C.: Marine20 - The Marine Radiocarbon Age Calibration Curve (0-55,000 cal BP), Radiocarbon, 62, 779–820, https://doi.org/10.1017/RDC.2020.68, 2020.

Henshilwood, C. S., d'Errico, F., and Watts, I.: Engraved ochres from the Middle Stone Age levels at Blombos Cave, South Africa, J. Hum. Evol., 57, 27–47, https://doi.org/10.1016/j.jhevol.2009.01.005, 2009.

Henshilwood, C. S., D'Errico, F., Van Niekerk, K. L., Coquinot, Y., Jacobs, Z., Lauritzen, S. E., Menu, M., and García-Moreno, R.: A 100,000-year-old ochre-processing workshop at Blombos Cave, South Africa, Science, 334, 219–222, https://doi.org/10.1126/science.1211535, 2011.

Henshilwood, C. S., van Niekerk, K. L., Wurz, S., Delagnes, A., Armitage, S. J., Rifkin, R. F., Douze, K., Keene, P., Haaland, M. M., Reynard, J., Discamps, E., and Mienies, S. S.: Klipdrift Shelter, southern cape, south africa: Preliminary report on the howiesons poort layers, J. Archaeol. Sci., 45, 284–303, https://doi.org/10.1016/j.jas.2014.01.033, 2014.

Henshilwood, C. S., d'Errico, F., van Niekerk, K. L., Dayet, L., Queffelec, A., and Pollarolo, L.: An abstract drawing from the 73,000-year-old levels at Blombos Cave, South Africa, Nature, 562, 115–118, https://doi.org/10.1038/s41586-018-0514-3, 2018.

Hernández-Almeida, I., Ausín, B., Saavedra-Pellitero, M., Baumann, K. H., and Stoll, H. M.: Quantitative reconstruction of primary productivity in low latitudes during the last glacial maximum and the mid-to-late Holocene from a global Florisphaera profunda calibration dataset, Quaternary Sci. Rev., 205, 166–181, https://doi.org/10.1016/j.quascirev.2018.12.016, 2019.

Hines, S. K. V., Bolge, L., Goldstein, S. L., Charles, C. D., Hall, I. R., and Hemming, S. R.: Little Change in Ice Age Water

https://doi.org/10.5194/egusphere-2024-2499
Preprint. Discussion started: 20 August 2024

Mass Structure From Cape Basin Benthic Neodymium and Carbon Isotopes, Paleoceanography and Paleoclimatology, 36, https://doi.org/10.1029/2021PA004281, 2021.

Jury, M.R., Valentine, H.R. and Lutjeharms, J.R.: Influence of the Agulhas Current on summer rainfall along the southeast coast of South Africa. J. Appl. Meteorol. Clim., 32(7), 1282-1287, https://doi.org/10.1175/1520-0450(1993)032%3C1282:IOTACO%3E2.0.CO;2, 1993.

Kohfeld, K. E., Graham, R. M., de Boer, A. M., Sime, L. C., Wolff, E. W., Le Quéré, C., and Bopp, L.: Southern Hemisphere westerly wind changes during the Last Glacial Maximum: Paleo-data synthesis, Quaternary Sci. Rev., 68, 76–95, https://doi.org/10.1016/j.quascirev.2013.01.017, 2013.

Kotov, S. and Pälike, H.: QAnalySeries: a cross-platform time series tuning and analysis tool, in: AGU Fall Meeting Abstracts, Vol. 2018, PP53D-1230, https://agu.confex.com/agu/fm18/meetingapp.cgi/Paper/349843, 2018.

Kylander, M. E., Ampel, L., Wohlfarth, B., and Veres, D.: High-resolution X-ray fluorescence core scanning analysis of Les Echets (France) sedimentary sequence: New insights from chemical proxies, J. Quat. Sci., 26, 109–117, https://doi.org/10.1002/jqs.1438, 2011.

Lazenby, M. J., Todd, M. C., and Wang, Y.: Climate model simulation of the South Indian Ocean Convergence Zone: Mean state and variability, Clim. Res., 68, 59–71, https://doi.org/10.3354/cr01382, 2016.

Li, M., Hinnov, L., and Kump, L.: Acycle: Time-series analysis software for paleoclimate research and education, Comput.. Geosci., 127, 12–22, https://doi.org/10.1016/j.cageo.2019.02.011, 2019.

Lisiecki, L. E. and Raymo, M. E.: A Pliocene-Pleistocene stack of 57 globally distributed benthic δ 18O records, Paleoceanography, 20, 1–17, https://doi.org/10.1029/2004PA001071, 2005.

Liu, W., Lu, J., Leung, L. R., Xie, S. P., Liu, Z., and Zhu, J.: The de-correlation of westerly winds and westerly-wind stress over the Southern Ocean during the Last Glacial Maximum, Clim. Dynam., 45, 3157–3168, https://doi.org/10.1007/s00382-015-2530-4, 2015.

Lombard, M., Wadley, L.Y.N., Deacon, J., Wurz, S., Parsons, I., Mohapi, M., Swart, J. and Mitchell, P.: South African and Lesotho stone Age sequence updated, S. Afr. Archaeol. Bull., 67(195), pp.123-144, https://www.jstor.org/stable/23631399, 2012.

Lougheed, B. C. and Obrochta, S. P.: MatCal: Open Source Bayesian ^{14}C Age Calibration in Matlab, J. Open Res. Softw., 4, 42, https://doi.org/10.5334/jors.130, 2016.

Lougheed, B. C. and Obrochta, S. P.: A Rapid, Deterministic Age-Depth Modeling Routine for Geological Sequences With Inherent Depth Uncertainty, Paleoceanogr. Paleocl., 34, 122–133, https://doi.org/10.1029/2018PA003457, 2019.

Ludwig, W. and Probst, J.L.: River sediment discharge to the oceans: present-day controls and global budgets, Am. J. Sci., 2, 265-295, https://doi.org/10.2475/ajs.298.4.265, 1998.

Maher, B. A., Prospero, J. M., Mackie, D., Gaiero, D., Hesse, P. P., and Balkanski, Y.: Global connections between aeolian dust, climate and ocean biogeochemistry at the present day and at the last glacial maximum, Earth-Science Rev., 99, 61–97, https://doi.org/10.1016/j.earscirev.2009.12.001, 2010.

https://doi.org/10.5194/egusphere-2024-2499
Preprint. Discussion started: 20 August 2024

Maslin, M. A. and Ridgwell, A. J.: Mid-Pleistocene revolution and the "eccentricity myth," Geol. Soc. Spec. Publ., 247, 19–34, https://doi.org/10.1144/GSL.SP.2005.247.01.02, 2005.

Mcbrearty, S. and Brooks, A. S.: The revolution that wasn't: A new interpretation of the origin of modern human behavior, J. Hum. Evol., 39, 453–563, https://doi.org/10.1006/jhev.2000.0435, 2000.

McCall, G. S. and Thomas, J. T.: Still Bay and Howiesons Poort Foraging Strategies: Recent Research and Models of Culture Change, Afr. Archaeol. Rev., 29, 7–50, https://doi.org/10.1007/s10437-012-9107-y, 2012.

Mcgee, D.: Glacial – Interglacial Precipitation Changes, Annu. Rev. Mar. Sci., 12, 525–557, https://doi.org/10.1146/annurev-marine-010419-010859, 2020.

Miller, C., Hahn, A., Liebrand, D., Zabel, M., and Schefuß, E.: Mid- and low latitude effects on eastern South African rainfall over the Holocene, Quaternary Sci. Rev., 229, 106088, https://doi.org/10.1016/j.quascirev.2019.106088, 2020.

Mourre, V., Villa, P., and Henshilwood, C. S.: Early Use of Pressure Flaking on Lithic, Science, 330, 659–662, https://doi.org/10.1126/science.1195550, 2010.

Partridge, T. C., Demenocal, P. B., Lorentz, S. A., Paiker, M. J., and Vogel, J. C.: Orbital forcing of climate over South Africa: A 200,000-year rainfall record from the Pretoria Saltpan, Quaternary Sci. Rev., 16, 1125–1133, https://doi.org/10.1016/S0277-3791(97)00005-X, 1997.

Pryor, E. J., Tangunan, D., van der Lubbe, H. J. L., Simon, M. H., and Hall, I. R.: Recommended centrifuge method: Specific grain size separation in the <63 µm fraction of marine sediments, MethodsX, 12, https://doi.org/10.1016/j.mex.2024.102718, 2024.

R Core Team: R: A language and environment for statistical computing: Foundation for Statistical Computing (Vienna, AT), available at: https:/www.r-project.org (last access: December 2022), 2013.

Reason, C. J. C. and Mulenga, H.: Relationships between South African rainfall and SST anomalies in the southwest Indian Ocean, Int. J. Climatol., 19, 1651–1673, https://doi.org/10.1002/(SICI)1097-0088(199912)19:15<1651::AID-JOC439>3.0.CO;2-U, 1999.

Reimer, P. J. and Reimer, R. W.: A marine reservoir correction database and on-line interface, Radiocarbon, 43, 461–463, https://doi.org/10.1017/s0033822200038339, 2001.

Rial, J. A.: Pacemaking the ice ages by frequency modulation of Earth's orbital eccentricity, Science, 285, 564–568, https://doi.org/10.1126/science.285.5427.564, 1999.

Sime, L. C., Kohfeld, K. E., Le Quéré, C., Wolff, E. W., de Boer, A. M., Graham, R. M., and Bopp, L.: Southern Hemisphere westerly wind changes during the Last Glacial Maximum: Model-data comparison, Quaternary Sci. Rev., 64, 104–120, https://doi.org/10.1016/j.quascirev.2012.12.008, 2013.

Simon, M. H., Arthur, K. L., Hall, I. R., Peeters, F. J. C., Loveday, B. R., Barker, S., Ziegler, M., and Zahn, R.: Millennial-scale Agulhas Current variability and its implications for salt-leakage through the Indian-Atlantic Ocean Gateway, Earth Planet. Sc. Lett., 383, 101–112, https://doi.org/10.1016/j.epsl.2013.09.035, 2013.

Simon, M. H., Ziegler, M., Bosmans, J., Barker, S., Reason, C. J. C., and Hall, I. R.: Eastern South African hydroclimate

https://doi.org/10.5194/egusphere-2024-2499
Preprint. Discussion started: 20 August 2024

over the past 270,000 years, Sci. Rep-UK., 5, 1–10, https://doi.org/10.1038/srep18153, 2015.

Singarayer, J. S. and Burrough, S. L.: Interhemispheric dynamics of the African rainbelt during the late Quaternary, Quaternary Sci. Rev., 124, 48–67, https://doi.org/10.1016/j.quascirev.2015.06.021, 2015.

Stuut, J. B. W., Prins, M. A., Schneider, R. R., Weltje, G. J., Fred Jansen, J. H., and Postma, G.: A 300-kyr record of aridity and wind strength in southwestern Africa: Inferences from grain-size distributions of sediments on Walvis Ridge, SE Atlantic, Mar. Geol., 180, 221–233, https://doi.org/10.1016/S0025-3227(01)00215-8, 2002.

Tangunan, D., Berke, M. A., Cartagena-Sierra, A., Flores, J. A., Gruetzner, J., Jiménez-Espejo, F., LeVay, L. J., Baumann, K. H., Romero, O., Saavedra-Pellitero, M., Coenen, J. J., Starr, A., Hemming, S. R., Hall, I. R., Barker, S., Brentegani, L., Caley, T., Charles, C. D., Crespin, J. G., Franzese, A. M., Han, X., Hines, S. K. V., Jimenez Espejo, F. J., Just, J., Koutsodendris, A., Kubota, K., Lathika, N., Norris, R. D., dos Santos, T. P., Robinson, R. S., Rolison, J. M., Simon, M. H., Tangunan, D., van der Lubbe, J. J. L., Yamane, M., and Zhang, H.: Strong glacial-interglacial variability in upper ocean hydrodynamics, biogeochemistry, and productivity in the southern Indian Ocean, Communications Earth and Environment, 2, https://doi.org/10.1038/s43247-021-00148-0, 2021.

Taylor, S. P., Patterson, M. O., Lam, A. R., Jones, H., Woodard, S. C., Habicht, M. H., Thomas, E. K., and Grant, G. R.: Expanded North Pacific Subtropical Gyre and Heterodyne Expression During the Mid-Pleistocene, Paleoceanography and Paleoclimatology, 37, 1–22, https://doi.org/10.1029/2021PA004395, 2022.

Thomson, J., Higgs, N. C., and Colley, S.: Diagenetic redistributions of redox-sensitive elements in northeast Atlantic glacial/interglacial transition sediments, Earth Planet. Sc. Lett., 139, 365–377, https://doi.org/10.1016/0012-821X(96)00031-3, 1996.

Todd, M. C., Washington, R., and Palmer, P. I.: Water vapour transport associated with tropical-temperate trough systems over southern Africa and the southwest Indian Ocean, Int. J. Climatol., 24, 555–568, https://doi.org/10.1002/joc.1023, 2004.

Torrence, C. and Compo, G. P.: A Practical Guide to Wavelet Analysis, B. Am. Meteorol. Soc., 79, 61–78, https://doi.org/10.1175/1520-0477(1998)079<0061:APGTWA>2.0.CO;2, 1998.

Uenzelmann-Neben, G. and Huhn, K.: Sedimentary deposits on the southern South African continental margin: Slumping versus non-deposition or erosion by oceanic currents?, Mar. Geol., 266, 65–79, https://doi.org/10.1016/j.margeo.2009.07.011, 2009.

Van Aken, H. M., Ridderinkhof, H., and De Ruijter, W. P. M.: North Atlantic deep water in the south-western Indian Ocean, Deep-Sea Res. Pt. I, 51, 755–776, https://doi.org/10.1016/j.dsr.2004.01.008, 2004.

Vazquez Riveiros, N. and Waelbroeck, C.: MD 225 / ACCLIMATE-2 cruise, RV Marion Dufresne, Campagnes Océanographiques Françaises, https://doi.org/10.17600/18001350, 2020.

Veres, D., Bazin, L., Landais, A., Toyé Mahamadou Kele, H., Lemieux-Dudon, B., Parrenin, F., Martinerie, P., Blayo, E., Blunier, T., Capron, E., Chappellaz, J., Rasmussen, S. O., Severi, M., Svensson, A., Vinther, B., and Wolff, E. W.: The Antarctic ice core chronology (AICC2012): An optimized multi-parameter and multi-site dating approach for the last 120 thousand years, Clim. Past, 9, 1733–1748, https://doi.org/10.5194/cp-9-1733-2013, 2013.

https://doi.org/10.5194/egusphere-2024-2499
Preprint. Discussion started: 20 August 2024

Weltje, G. J. and Tjallingii, R.: Calibration of XRF core scanners for quantitative geochemical logging of sediment cores: Theory and application, Earth Planet. Sc. Lett., 274, 423–438, https://doi.org/10.1016/j.epsl.2008.07.054, 2008.

Wurz, S.: Variability in the Middle Stone Age lithic sequence, 115,000-60,000 years ago at Klasies River, South Africa, J. Archaeol. Sci., 29, 1001–1015, https://doi.org/10.1006/jasc.2001.0799, 2002.

Wurz, S.: The Transition to Modern Behavior, Nature Education Knowledge, 3(10), https://www.nature.com/scitable/knowledge/library/the-transition-to-modern-behavior-86614339/, 2012.

Yu, J., Menviel, L., Jin, Z. D., Anderson, R. F., Jian, Z., Piotrowski, A. M., Ma, X., Rohling, E. J., Zhang, F., Marino, G., and McManus, J. F.: Last glacial atmospheric CO2 decline due to widespread Pacific deep-water expansion, Nat. Geosci., 13, 628–633, https://doi.org/10.1038/s41561-020-0610-5, 2020.

Zabel, M., Schneider, R. R., Wagner, T., Adegbie, A. T., De Vries, U., and Kolonic, S.: Late quaternary climate changes in central Africa as inferred from terrigenous input to the Niger fan, Quaternary Res., 56, 207–217, https://doi.org/10.1006/qres.2001.2261, 2001.

Ziegler, M., Simon, M. H., Hall, I. R., Barker, S., Stringer, C., and Zahn, R.: Development of Middle Stone Age innovation linked to rapid climate change, Nat. Commun., 4, 1905–1909, https://doi.org/10.1038/ncomms2897, 2013.